MONGE, JOSUÉ ROBERTO, M.S. Constructing Velocity Distributions in Crossed-Molecular Beam Studies using Fourier Transform Doppler Spectroscopy. (2012) Directed by Liam M. Duffy. 74 pp.

The goal of our scattering experiments is to derive the distribution the differential cross-section and elucidate the dynamics of a bimolecular collision via pure rotational spectroscopy. We have explored the use of a data reduction model to directly transform rotational line shapes into the differential cross section and speed distribution of a reactive bimolecular collision. This inversion technique, known as Fourier Transform Doppler Spectroscopy (FTDS), initially developed by James Kinsey [1], deconvolves the velocity information contained in one-dimensional Doppler Profiles to construct the non-thermal, state-selective three-dimensional velocity distribution. By employing an expansion in classical orthogonal polynomials, the integral transform in FTDS can be simplified into a set of purely algebraic expressions technique; i.e. the Taatjes method [2]. In this investigation, we extend the Taatjes method for general use in recovering asymmetric velocity distributions. We have also constructed a hypothetical asymmetric distribution from adiabatic scattering in Argon–Argon to test the general method. The angle- and speed-components of the sample distribution were derived classically from a Lennard-Jones 6-12 potential, with collisions at $60\,m$eV, and mapped onto Radon space to generate a set of discrete Doppler profiles. The sample distribution was reconstructed from these profiles using FTDS. Both distributions were compared along with derived total cross sections for the Argon–Argon system. This study serves as a template for constructing velocity distributions from bimolecular scattering experiments using the FTDS inversion technique.

CONSTRUCTING VELOCITY DISTRIBUTIONS IN CROSSED-MOLECULAR

BEAM STUDIES USING FOURIER TRANSFORM DOPPLER

SPECTROSCOPY

by

Josué Roberto Monge

A Thesis Submitted to
the Faculty of the Graduate School at
The University of North Carolina at Greensboro
in Partial Fulfillment
of the Requirements for the Degree
Master of Science

Greensboro
2012

Approved by

_____
Committee Chair

To my loved ones who have been there every step of the way...

APPROVAL PAGE

This thesis has been approved by the following committee of the Faculty of The Graduate School at The University of North Carolina at Greensboro.

Committee Chair _____
Liam M. Duffy

Committee Members _____
William J. Gerace

_____
Robert M. Whitnell

_____
Date of Acceptance by Committee

_____
Date of Final Oral Examination

ACKNOWLEDGMENTS

I am truly indebted to Prof. Liam Duffy for the encouragement and guidance throughout this endeavor. You have been a great mentor and friend stretching back to my gutsy experience as an undergraduate research assistant in your laboratory. You have encouraged me to purse this challenging field of study and believed in me during the toughest times of this project (while lost in the "darkness"). I would also like to express my gratitude to Prof.'s Robert Whitnell and William Gerace for not only partaking as committee members, but for their assistance and expertise at critical points of this project; without your help, this endeavor would have stayed at a standstill. Thank you both for your time and thoughtful consideration. In addition, I would like to thank the Department of Chemistry & Biochemistry at the University of North Carolina at Greensboro (UNCG) for the financial and moral support throughout my undergraduate and graduate careers. The faculty and staff have always been kind and accepting, making it my home away from home for the past six years.

Finally, I want to acknowledge my family and my better-half Emily, for their love and support for my past and present adventures; without your strength and words of encouragement this labor would never have happened.

TABLE OF CONTENTS

LIST OF FIGURES

vi

CHAPTER I

OVERVIEW

Molecular reaction dynamics is the study of individual chemical reactions on the atomic length and time scales [3]. Tools in mathematical and experimental physics are used to probe and characterize the collision dynamics associated in a chemical transformation. This information is used to predict and control how energy is distributed among translation, rotation, and vibration of the reaction products. In the Duffy lab at the University of North Carolina at Greensboro, we explore the use of a data reduction model called *Fourier Transform Doppler Spectroscopy*, FTDS, to extract vector information from state-specific reaction products for use in cross-molecular beam experiments. In this chapter, an outline of the thesis is provided with a brief overview of each of the subsequent chapters.

1.1 Thesis Outline

Chapter II provides a brief survey into Molecular reaction dynamics. Common experimental tools are discussed in detail and include time-resolved laser spectroscopy and a variety of crossed-molecular beam experiments that differ in detection. Extraction of dynamical information from these methods are briefly explained. The Duffy lab crossed-molecular beam machine is discussed along with its unique detection scheme and data interpretation. In this chapter, we introduce FTDS as our method to construct product angular and speed distributions from Doppler line-

shapes of state-selective reaction product(s). In chapter 3.3 a background into FTDS explains the motivation for the technique along with a detailed explanation of the Doppler technique. A derivation of FTDS is provided along with a general method for reconstructing cylindrically symmetric distributions analytically. A symmetric velocity distribution from a parallel-type transition in photodissociation is modeled and reconstructed using the general method. FTDS has been used to construct many photodissociative processes due to the simplicity and symmetry of these systems. In chapter IV, we explore the use of FTDS on asymmetry velocity distributions acquired from crossed-molecular beam experiments. We model an adiabatic Argon–Argon interaction and construct an asymmetric sample distribution classically from a spherically symmetric intermolecular potential. The mechanics of the problem are detailed and the differential cross section of the Argon–Argon collision system is computed from empirically derived parameters and compared for accuracy. In this exercise, we attempt to simulate lineshapes from a velocity distribution we could observe using our crossed-molecular beam apparatus. The profiles are fit with Hermite and Legendre polynomials and used to reconstruct the initial forward problem. A procedure for reconstructing distributions using our experimental set-up is discussed including limitations to the technique. Chapter V includes a summary and concluding remarks. An explicit derivation of the FTDS inversion technique and the general method are provided in Appendices A and B, respectively.

CHAPTER II

INTRODUCTION

2.1   Molecular Scattering

Molecular beam scattering studies have been used for decades to characterize the intermolecular forces and dynamics that govern chemical reactivity [3–9]. Considered the low energy (i.e. interaction energies <10 eV) antithesis of scattering experiments conducted at CERN's Large Hadron Collider, molecular beam scattering studies provide an account of the underlying forces involved in an observable chemical reaction. The typical experiment consists of crossing two gas beams under single collision conditions and observing the nascent scattering products, Figure 1.
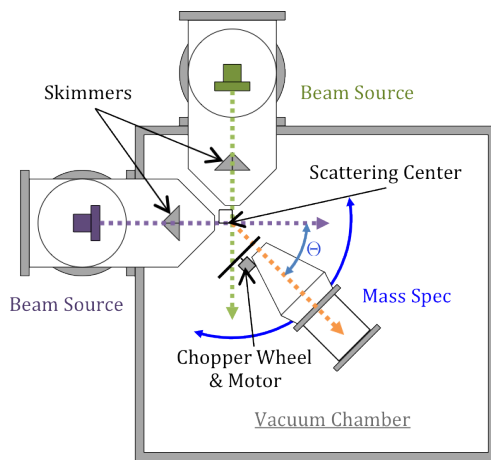
Figure 1. Crossed molecular beam apparatus. Detection of reaction products is a function of laboratory angle Θ.

Single collision conditions translate into an experimental set-up under high vacuum ($<10^{-6}$ torr) with highly collimated, differentially pumped beam sources. This arrangement ensures **a.)** the likelihood of a single interaction between molecular components of the intersecting beams (i.e. two-body interaction) and **b.)** the observation of its unaltered products.

The interacting bodies exert a force on one another that can alter the direction, motion, and composition of its participants. In terms of chemistry, the interaction (referred hereinafter as a "collision") results in the energy, mass, or charge exchange between the reactants. The reaction can be pictured as an inertial frame with two bodies approaching a collision point along a straight line, Figure 2.
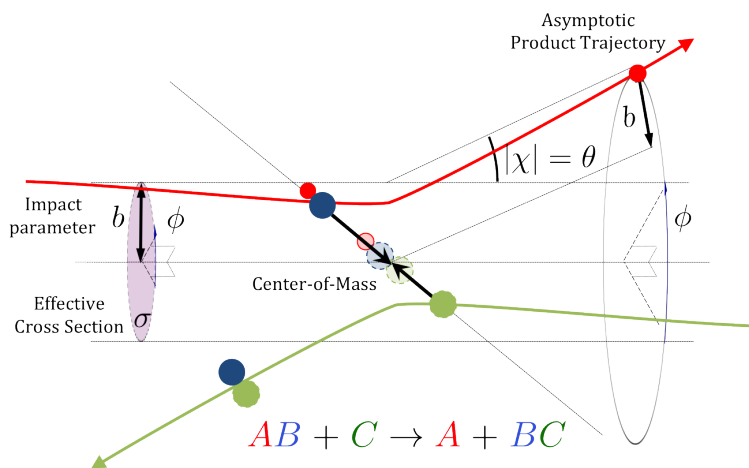
Figure 2. Two-body collision of $AB + C \rightarrow A + BC$ reaction.

The collision prompts the chemical transformation and potentially redirects the product(s) from the reactant trajectories. The angle formed between the initial and final

trajectories, i.e. the deflection angle χ, is characteristic of the force and impact parameter, b; the perpendicular distance from the target-body to the initial trajectory of the incident-body.

The forces that constitute an observable chemical transformation can be determined by tracing the trajectories of the scattering products about the collision point. These "chemical" forces, typically weak electrostatic interactions, are assumed to be central (spherically symmetric) and conservative (explicitly do not depend on time or velocity). As a consequence of such a force field, the total mechanical energy and angular momentum of the system are constants of motion and have a unique effect on the observed scattering [10]; see Section 4.1 for further discussion.

Observing the motion of individual atoms as their parent molecules collide would provide a complete picture of the forces and dynamics involved in a chemical reaction. This information can be available using femtosecond pump-probe spectroscopy, i.e. the "molecular microscope". The technique involves splitting a laser beam in two, utilizing one beam to initiate the interaction (i.e. the "pump" laser), and probing the time evolving change with the other beam, Figure 3. A series of laser probe delays can obtain plot the time-progression, for example, of a bond-breaking or forming in a chemical reaction. But an inherent difficulty exists in examining bimolecular collisions using this real-time clocking technique [3; 11–13]. If reactive bimolecular collisions occur on a nano- to microsecond timescale, the probability a femtosecond pump pulse interacts with the reactants at the very moment they collide is very low; about one in 10,000. This makes it virtually impossible to accurately determine the

"zero-of-time" in a crossed-molecular beam experiment, since there are no synchronized reactive collisions between the "pumped" (state-selected) reactants. Conversely, a crossed-molecular beam set-up using a rotatable time-of-flight mass spectrometer (TOF-MS) provides a means to "visualize" the details of a chemical reaction [5].
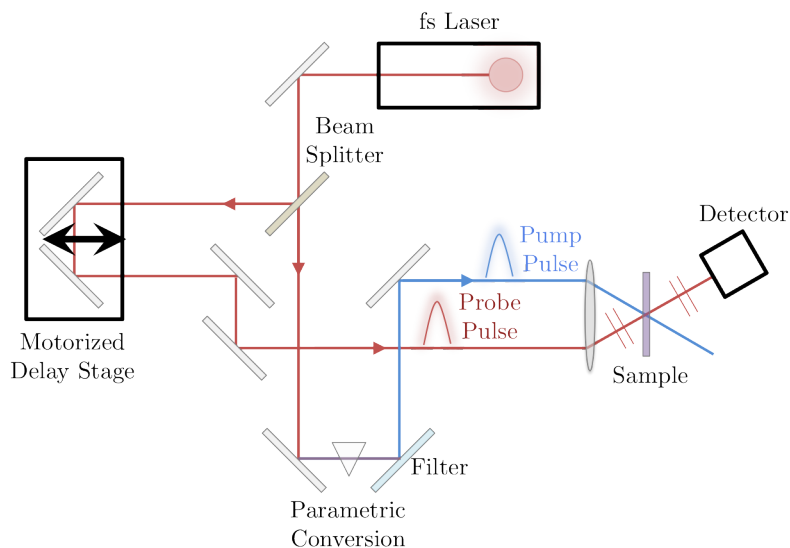
Figure 3. Time-resolved pump-probe spectroscopy set-up.

2.2 Crossed Molecular Beam Machine

In a crossed-molecular beam experiment, the two beam sources are stationary and crossed at 90°. The beams are produced when a high-pressure gas traverses a short-converging nozzle into an evacuated chamber, Figure 4. As the gas particles exit the nozzle, they undergo an adiabatic expansion which converts the random thermal motion of a hot static gas into the forward directed flow of a cold, supersonic beam of molecules [14–16]. The molecular beams are collimated and differentially pumped

in order to remove the highly divergent and rotationally hot parts of the free jet expansion, allowing only the coldest part of the beam to enter the interaction chamber, Figure 1.
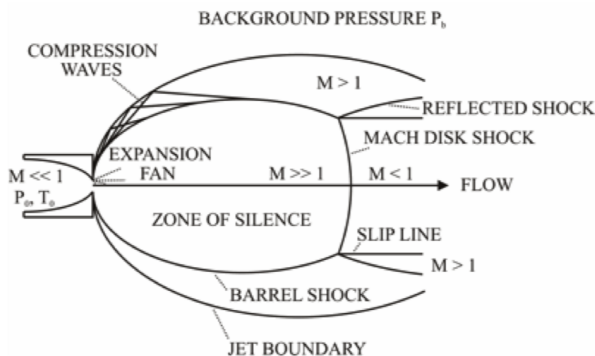
Figure 4. Free jet expansion in short-converging nozzles. Reprinted with permission from *Atomic and molecular beam methods, vol. 1*, Copyright 1988, Oxford University Press. [14]

Detection of nascent scattering products is obtained via mass spectrometry. Briefly, neutral molecules enter a rotatable mass spectrometer at a well-defined solid angle, $\Delta\Omega(\Theta, \Phi)$. Ions are produced via electron impact (at ~100 eV) and extracted into a quadrupole mass filter. Time-of-flight (TOF) spectra are obtained by synchronizing a chopper wheel at the entrance of the detector with the signal acquisition from the ion counter. Nicknamed the "universal" machine for its ability to detect ionizable species, the time- and angle-resolved measurements of this set-up trace the nascent product trajectories (relative to the collision center) and resolves the translational energy release of the reaction. Construction of a Newton (or velocity vector) diagram, Figure 5, from the crossed-beam geometry provides for a kinematic analysis of

the reaction. In Figure 5, the velocity vectors in the laboratory and center-of-mass frames are denoted v and u, respectively.
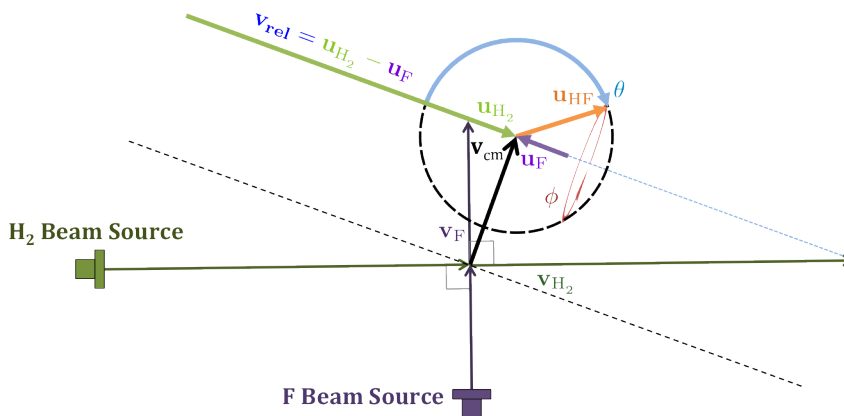
Figure 5. Newton diagram of the F + H_2 → HF + H reaction.

Since the measurements are acquired in the laboratory frame, a transformation of coordinates (or Jacobian) is necessary to view the scattering products from the collision point (i.e. the center-of-mass frame); Figure 6. In the center-of-mass frame, the product scattering distribution contains cylindrical symmetry about the relative velocity vector, $\mathbf{v_{rel}} = \mathbf{u}_{H_2} - \mathbf{u}_F$, i.e. the line joining the centers of the reactants.

$$J = \begin{bmatrix} \dfrac{\partial F_1}{\partial x_1} & \cdots & \dfrac{\partial F_1}{\partial x_n} \\ \vdots & \ddots & \vdots \\ \dfrac{\partial F_m}{\partial x_1} & \cdots & \dfrac{\partial F_m}{\partial x_n} \end{bmatrix}$$
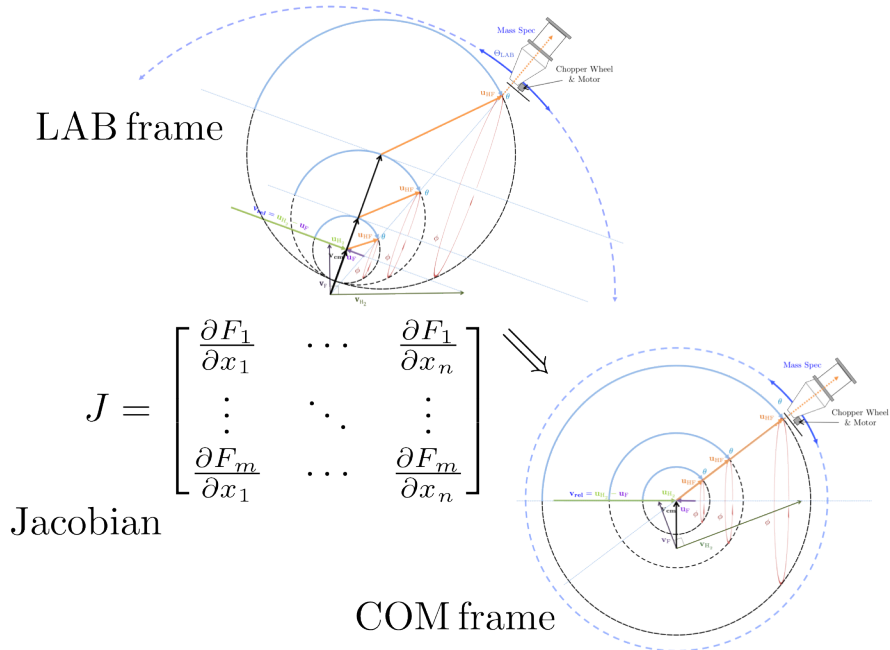
Jacobian

Figure 6. Jacobian of the transformation from LAB to COM frame. In this schematic, a hypothetical velocity distribution in the LAB frame is transformed into the COM via Jacobian matrix.

By virtue of energy conservation, the accessible quantum ro-vibrational states (E'_{int}) are determined by **1.)** the observed recoil velocity of the collision products(E'_{trans}), **2.)** the internal energy of the reactants (E_{int}) and their relative translational motion in the center-of-mass frame (E_{trans}), and **3.)** the standard reaction energy change (i.e. the difference in bond dissociation energies, ΔE_0); equation II.1.

$$E_{total} = E'_{int} + E'_{trans} = E_{int} + E_{trans} - \Delta E_0 \tag{II.1}$$

The possible spectrum of recoil velocity vectors form a discrete set of expanding concentric spheres, known as Newton spheres (Figure 7), which expand along the

center-of-mass velocity. These spheres each correspond to a unique partitioning of
the total energy, E_{total}, between translational and internal states, relating the radius
of the sphere to a particular internal mode of motion.
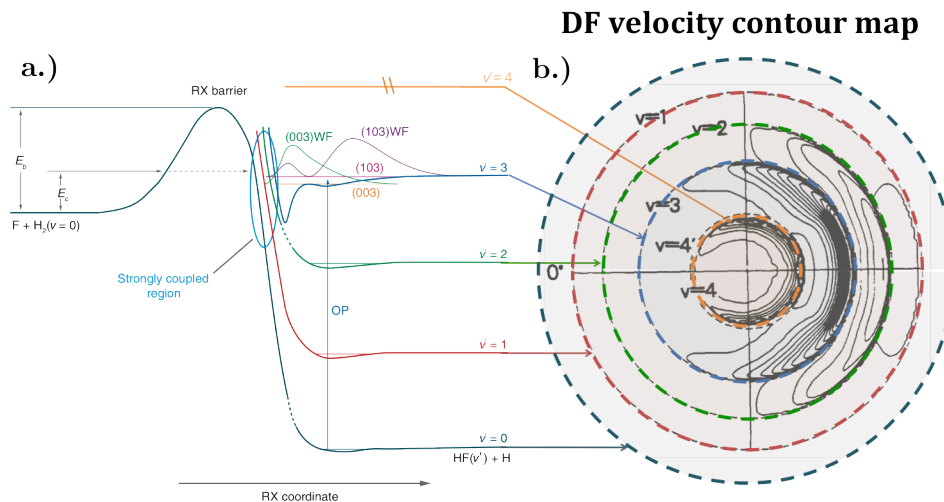
Figure 7. Reaction coordinate for the F + H$_2$ → HF + H reaction.
a) Feshbach resonance-mediated reaction mechanism for F + H$_2$ with two resonance
states trapped in the HF(v' = 3)–H' vibrational adiabatic potential well; one dimen-
sional wave functions are provided for (003) and (103). Republished with permission
of Annual Reviews, from *Annu. Rev. Phys. Chem. 2007, 58: 433-59*; permission
conveyed through Copyright Clearance Center, Inc. [6]
b) Center-of-mass frame velocity-flux contour map for the F + D$_2$ reaction at 1.82
kcal/mol. Adapted from *J. Chem. Phys. 1985, 82: (7), 3067-77*. Copyright 1985,
American Institute of Physics with permission from author. [5]

In Figure 7, the outlined spheres (vibrational states at maximum recoil velocity)
map internal states on the product contour map to those on the one-dimensional po-
tential energy profile. The contours between adjacent spheres represent the remaining
energy disposal between translational and rotational states and the probability they

10

appear at specific angles and speeds. Together the translational energy and angular distributions of the scattering products reveal details of the reaction's potential energy surface; e.g. its shape, barriers, the role and geometry of short-lived molecular states during scattering, etc.

A major goal in molecular beam scattering studies is to understand how electronic and nuclear motions are coupled in elementary inelastic and reactive collisions. This information is derived from the observed distribution in deflection angles (referred to as the *differential cross section*) that arises in, for example, reactive molecular collisions, molecular photodissociation, weakly-bound complexes, etc. Ideally, the empirical data is directly inverted or transformed into its associated potential energy function (the so-called inverse quantum scattering problem). But such a procedure is ill-posed, i.e. conditions do not satisfy either existence, uniqueness, or continuity with respect to the data and the experimental error [17; 18]. Instead, the empirical data is used to ameliorate *ab initio* quantum calculations of the reaction's potential energy surface, also known as the forward convolution technique. In addition to its fundamental importance, gas phase chemical dynamics enable the interpretation of many important macroscopic phenomena. These include applications in practical disciplines such as combustion, atmospheric chemistry, astrophysics, plasmas, laser physics, etc. [9].

2.3 An Alternative Method for Obtaining the Differential Cross Section

In Prof. Liam Duffy's lab at UNCG, we have designed and built a new crossed-molecular beam machine and are currently in the testing stages. Instead of stationary

crossed-molecular beam sources, as in the universal machine (Figure 1), we have constructed a rotatable, differentially pumped molecular beam set-up, Figure 8a. The new set-up permits each arm (i.e. aluminum housing that suspends a pulsed beam source and its skimmer about the center of the chamber) to rotate independently from one another. This provides the ability to adjust the relative collision energy of the reactants without altering the internal state distribution of the colliding species [19]. The scattering products are detected using a direct absorption scheme, consisting of passing linearly polarized microwave radiation through polar molecules. A liquid-Helium cooled InSb hot-electron bolometer chip detects the evolving transient absorption signals, which are used to generate rotational line-shapes in frequency space, referred to as Doppler profiles [20].

The immediate goal of our scattering experiments is to obtain the velocity distribution, and hence the differential cross section, from elementary reactive collisions using our direct absorption set-up. In order to do so, we must explore the use of a mathematical model to transform the acquired data, i.e. our Doppler profiles, into the velocity distribution of a reaction. *Fourier Transform Doppler Spectroscopy* (FTDS) is an inversion technique that allows the construction of a state-selective three-dimensional velocity distribution from discrete one-dimensional Doppler profiles [1]. In our crossed-molecular beam set-up, fixing the collision energy of the reaction and rotating the arms synchronously (relative to the millimeter wave probe) can achieve this (see insert in Figure 8a).
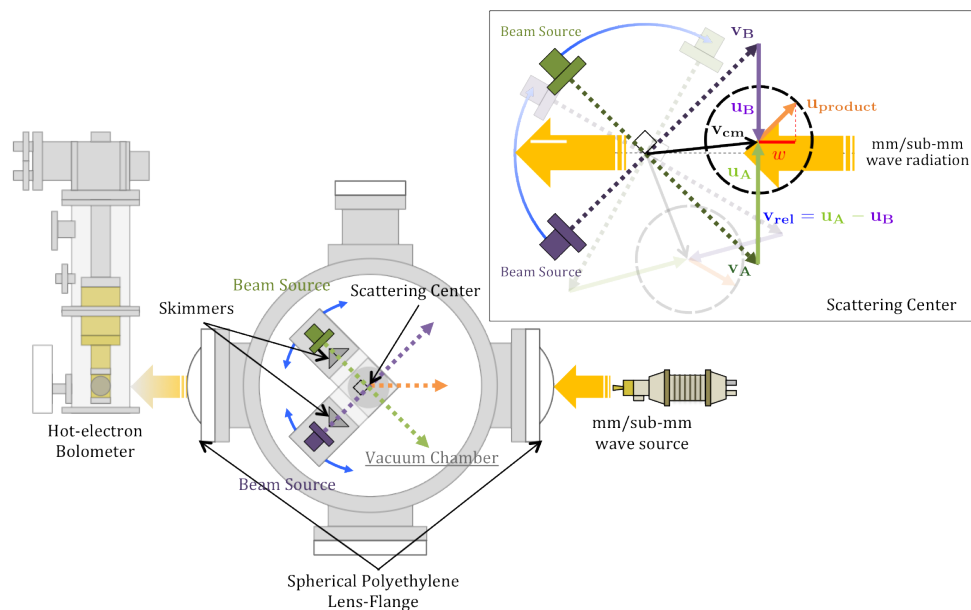
(a) Doppler Machine layout. Insert: Sample Newton Diagram
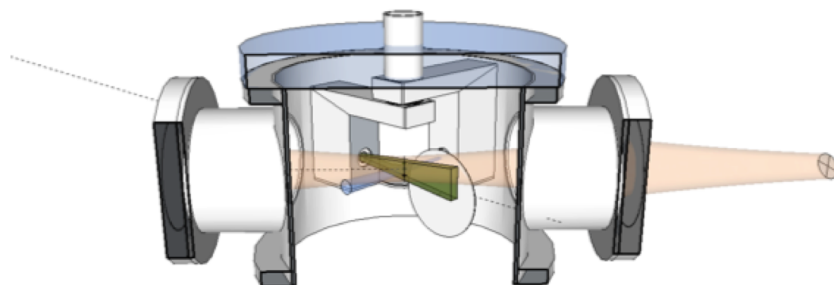
(b) Cut-through of set-up [19]

Figure 8. Illustration of the Duffy Lab Doppler Machine. The rotatable arms each house a collimated and differentially pumped molecular beam source.

The FTDS inversion technique and our experimental set-up would enable us to observe angle-resolved rotational line-shapes and construct the three-dimensional velocity distribution of an individual product rotational state.

In order to confirm the utility of the FTDS inversion technique with distributions arising from bimolecular scattering experiments, we intend to construct the forward scattering problem. We opt for a well-studied scattering system with known collision cross-sections and angular distributions at well-defined collision energies. Our intent is to construct the angular distribution of elastic Argon–Argon scattering from an intermolecular potential with laboratory-like system constraints. We will derive the total cross section and compare our theoretical results to experimental studies. From these constraints, we will build a non-thermal product velocity distribution from speed and angle-dependent components. A set of Doppler profiles will be extracted from the forward constructed velocity distribution and an expansion in classical orthogonal polynomials will be used to fit the profiles. The polynomial expansion enables the integral transform in FTDS to be solved analytically, a procedure developed by Taatjes *et al.* [2], and makes the procedure computationally robust. We extend this method to incorporate both odd and even Hermite and Legendre terms in our polynomial expansion, resulting in a modified analytical expression for the inversion procedure. In this investigation, we attempt to fit Doppler profiles with our expansion scheme using the coefficients to recover the simulated velocity distribution in in Argon–Argon elastic scattering. This study will serve as a template for constructing velocity distributions for future bimolecular scattering experiments in the Duffy lab.

CHAPTER III

FOURIER TRANSFORM DOPPLER SPECTROSCOPY

3.1 Background

Fourier Transform Doppler Spectroscopy (FTDS) is an inversion technique that recovers the three-dimensional velocity distribution from a collection of one-dimensional Doppler profiles. In 1977, Prof. James Kinsey at MIT developed the technique as an *alternative* to resolving speed distributions of the scattering products via time-of-flight mass spectrometric (TOF-MS) analysis [1; 7]; see Section 2.2 for a brief summary. Obstacles related to TOF-MS lie in compiling and interpreting the scattering data. Data acquisition can be a lengthy process involving multiple TOF scans for each accessible angle in the laboratory frame (which can span a 120° range). Angle-resolved speed distributions are derived from the TOF scans, but a Jacobian is necessary to transform the laboratory frame data into the reaction's center of mass frame. This operation enables the construction of a product velocity-flux contour map (e.g. Figure 6). Another shortcoming of this detection scheme is its inability to resolve internal state information directly from the detected species. This quantum state information is inferred from the speed distribution and its implied energy disposal about the center-of-mass, Figure 7. In contrast, FTDS provides a framework to transform a set of quantum state resolved measurements into the full velocity distribution of a scattering experiment in the center-of-mass frame [1; 2; 21; 22].

3.2　The Doppler Technique

FTDS involves the use of the Doppler technique to observe resonance absorption or emission of electromagnetic radiation by the scattered product(s). The process is best described in a spherical frame with products emanating from the origin (i.e. collision/center-of-mass point) with a variety of recoil velocities, $\mathbf{v}(v, \theta, \phi)$, Figure 9.
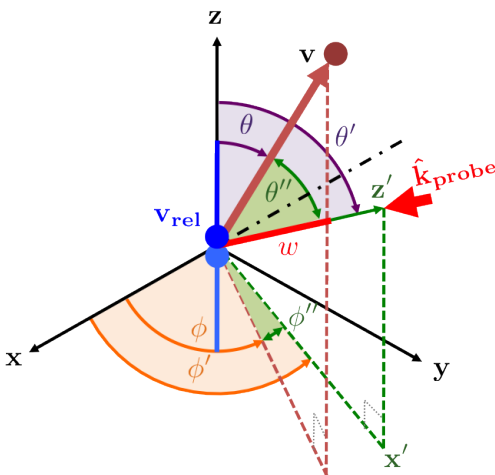
Figure 9. Space-fixed coordinate system for a bimolecular collision.

The state specific collision products are interrogated along the probe source direction, denoted $\hat{\mathbf{k}}_{\mathbf{probe}}$, defined by a coordinate transformation from the (xyz) system to a new (x'y'z') where the z'-axis points along $\hat{\mathbf{k}}_{\mathbf{probe}}$. Such a transformation maps the velocity information in the (xyz) system onto the new (x'y'z') sytem in the form of a scalar projection, equation III.1.

$$\mathbf{v} \cdot \hat{\mathbf{k}}_{\mathbf{probe}} = \|\mathbf{v}\| \cos \theta'' = w \tag{III.1}$$

16

Probe beam attenuation is observed when the orientation of the transition dipole moment within the molecule $\boldsymbol{\mu}$ and the polarization of the probing radiation $\mathbf{E_{probe}}$ are aligned [23; 24]. For the simplest case, the reaction products are considered structureless particles with an isotropic distribution of $\boldsymbol{\mu}$. Therefore, probing these scattering products at a fixed direction with different linearly polarized beams would produce the same spatial anisotropy; we will consider this case in the discussion below. The relation in equation III.1 is further complicated when considering molecular polarization and vector coupling between $\mathbf{v}$, $\boldsymbol{\mu}$, $\mathbf{E_{probe}}$, and the angular momentum vector $\mathbf{J}$ of the scattering product.

The geometric argument in equation III.1 also has a corresponding spectroscopic one. Interaction of the wave/probe with the particle depends on its relative motion with respect to the wave source. For example, if the particle has no velocity component relative to the direction of the wave source, the particle will absorb or emit radiation at the prescribed "rest" transition frequency, ν_0, Figure 10. Any velocity component along the direction of the source will correspond to a "shift" in the resonance rest frequency, known as the Doppler shift, $\Delta\nu$; equation III.2.

$$\nu = \nu_0(1 - \frac{w}{c}) \implies w = -\frac{\Delta\nu}{\nu_0}c \qquad (\text{III.2})$$
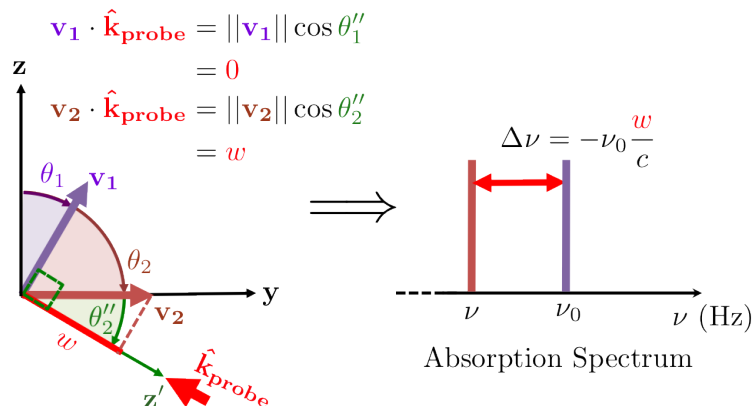
Figure 10. Doppler shifts of two velocities probed on the same plane.

Using a tunable frequency source to interrogate state specific collision products, the Doppler technique can directly probe a distribution of recoil velocities (or Newton sphere) arising from elementary chemical reactions. These inner product measurements or tomographic "slices" are projections that approximate the cumulative measurement of the product velocity distribution. The standard spectroscopic probing techniques are laser-induced fluorescence (LIF) and resonance-enhanced multiphoton ionization (REMPI) detection. Both consist of pumping a state-selective collision product with a tunable frequency source (e.g. a laser), but differ in detection scheme. In LIF, pumping a state-selected collision product takes the inner product measurement of the velocity vector field by observing the fluorescence of the probed molecules with the use of a photomultiplier tube (PMT) [1; 23]. REMPI further ionizes the pumped/state-selected products with a second laser and accelerates the resulting product ions into a multichannel plate (MCP) for spatial and TOF analysis; much like the universal machine, but with rotational resolution [25].

18

3.3 Tomographic Reconstruction of the Velocity Distribution

Tomographic determination of the state selective product recoil distribution is achieved by a discrete set of inner product measurements or Doppler profiles. The Radon transform provides the appropriate mathematical formalism for this tomographic reconstruction, equation III.3.

$$D(w; \theta', \phi') = \int \mathrm{d}^3\mathbf{v}\, F(\mathbf{v})\, \delta[w - \mathbf{v} \cdot \hat{\mathbf{k}}_{\mathbf{probe}}] \tag{III.3}$$

Here the Radon transform of the three-dimensional velocity vector field, $F(\mathbf{v})$, corresponds to the measured Doppler profile, $D(w; \theta', \phi')$, at specific polar and azimuthal angles (θ' and ϕ', respectively) about the collision center, Figure 9.

The inverse Radon transform would directly recover the desired velocity vector field from acquired Doppler profiles, but this method is difficult to derive and implement [26]. Instead, Kinsey applied the so-called Fourier synthesis method [27]. This inversion technique relates the Radon space $\mathfrak{R}$ projection of $F(\mathbf{v})$, taken along θ' and ϕ', to a "slice" of $F(\mathbf{v})$ in Fourier space $\mathfrak{F}_{1D}^{-1}$ at the same angles; a result known as the central-slice theorem. Therefore, recovery of the velocity vector field can be obtained by taking the three-dimensional inverse Fourier transform $\mathfrak{F}_{3D}^{-1}$ of a collection of slices in Fourier space, equation III.4. This procedure is illustrated in Figure 11.

$$F(\mathbf{v}) = \int \mathrm{d}^3\mathbf{k}\, G(\mathbf{k})\, e^{2\pi i (\mathbf{k} \cdot \mathbf{v})} \tag{III.4}$$
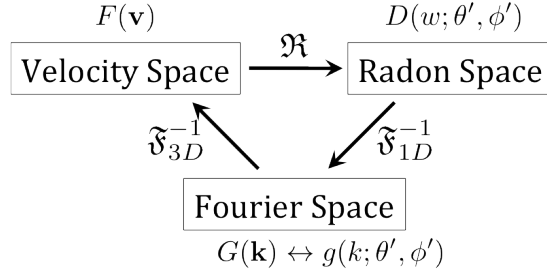
Figure 11. Flow-chart of FTDS inversion procedure.

A complete derivation of Kinsey's FTDS inversion procedure can be found in Appendix A. For brevity, only key expressions will be discussed in this section.

If a vector field is known to be either irrotational or solenoidal, then fewer inner product measurements are required to recover the vector field [27]. In our scattering problem (depicted in Figure 2), we introduced an *a priori* assumption regarding the angular distribution function. If we assume our colliding particles experience a central conservative force, the resulting recoil velocity distribution will exhibit cylindrical/axial symmetry along the relative velocity vector. The symmetry afforded by this problem can simplify the three-dimensional Fourier transform in equation III.4, into the product of a one-dimensional Fourier transform and a radially symmetric two-dimensional Fourier Transform in the traverse plane [28]. The latter is also referred to as a Hankel Transform, which contains a zeroth order Bessel function of the first kind, $J_0(z)$; encompassing the axial symmetry of the collision, equation III.5.

$$
F(v, \theta) = 2\pi \int_0^\infty \mathrm{d}k \, k^2 \int_0^{2\pi} \mathrm{d}\theta' \sin \theta' J_0(2\pi k v \sin \theta' \sin \theta) \, g_{cyl}(k; \theta') \, e^{2\pi i (kv) \cos \theta' \cos \theta}
$$

$$
(\text{III.5})
$$

Aside from the increased versatility, sensitivity, and specificity afforded by the Doppler technique, the main advantage of FTDS over TOF-MS detection is its gain in signal to noise from the so-called *Fellgett's* advantage [1]. In TOF-MS detection, the signal intensity of a TOF spectrum is proportional to the number of molecules detected in a small solid angle, $\Delta\Omega$, subtended from the detector opening. Comparatively, the multiplexed signal from a Doppler profile is attributed to the total number of resonant molecules traversing the probe. This phenomenon is irrespective of the molecule's direction, since the resonant particles all have a velocity component parallel to the radiation probe; see equation III.1. Since FTDS maps data onto Fourier space, digital filtering and image-enhancement techniques can readily remove unwanted convolutions [29]. Artifacts, such as broadening effects due to laser linewidth, shot noise, etc., can be removed by dividing their frequency response function from the acquired signal. Characteristics of the unwanted convolution must be understood with great accuracy and precision, since their removal can prompt drastic alterations to the signal.

3.4 A General Method for Reconstructing Cylindrically Symmetric Distributions

Due to the discrete nature of the Doppler profiles, the Fourier transform in equation III.5 can be evaluated numerically. But random noise in the experimental data (corresponding to high-frequency harmonics) can lead to excessive loss of information and/or numeric instability of the inverse transform [22; 27]. Alternatively, a functional form for the Doppler profiles enable the inverse Fourier transform to be

solved analytically. Using Gaussians for their Doppler profile fitting function, Kinsey and coworkers were the first to document a quantum state-resolved product velocity distribution via the FTDS inversion procedure [22; 30]. They examined the H + NO_2 reactive collision and derived a product velocity distribution in good agreement with TOF-MS constructed distributions. But much of the literature on FTDS is related to photo-induced half-collision processes (molecular photodissociation) [31–37]. The dynamics associated with full (i.e. bimolecular) collisions and half-collisions are identical, but differ slightly in the experimental set-up and its interpretation in the space-fixed inertial frame. Full bimolecular collisions contain a cylindrically symmetric scattering distribution about the relative velocity vector; i.e. the velocity along the line joining the scattering partner's centers (z-axis in Figure 9). In half-collision experiments, a molecular beam source is crossed with a dissociation laser. Fragmentation occurs when the electric vector of the photolysis light $\mathbf{E_{diss}}$, the transition dipole moment $\boldsymbol{\mu}$, and the dissociation bond axis of the molecule are aligned in a particular manner [23; 24]. Therefore, the direction of fragment departure, which defines the recoil velocity vector $\mathbf{v}$, bears a fixed angular relationship with the parent molecule's transition dipole moment $\boldsymbol{\mu}$. For example, in a parallel-type transitions, the electric vector and transition dipole are aligned parallel to the dissociation bond axis, giving rise to a cylindrically symmetric scattering distribution about the electric vector; i.e. the z-axis in Figure 12.
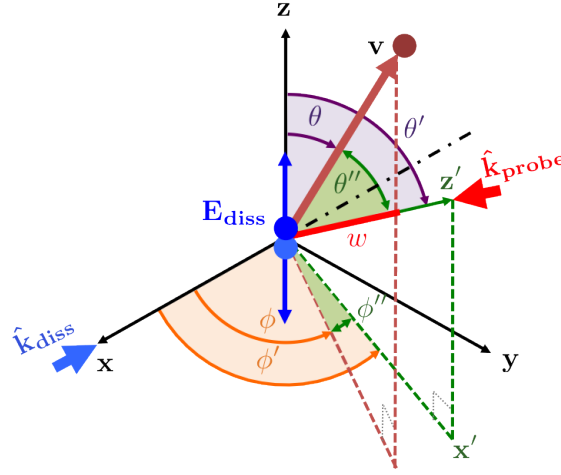
Figure 12. Space-fixed coordinate system for a parallel-type transition.

State specific photofragments are interrogated with a probe laser, $\hat{\mathbf{k}}_{\mathbf{probe}}$, whose direction is defined by Euler angles θ' and ϕ' relative to the dissociation laser's electric vector, $\mathbf{E}_{\mathbf{diss}}$.

In recovering product velocity distributions from half-collision processes using FTDS, implementation of a fitting function is common practice. Since Doppler profiles are typically symmetric in half-collision processes, the fitting function must be even and have a limit of zero outside the data range. In general, Gaussian or Gaussian-like functions can accurately represent the data and carry out the entire problem analytically [30; 33; 36]. Another fitting scheme assumes a specific functional form for $F(\mathbf{v})$ [31; 37]. If the product velocity distribution is separable into speed and angle components, it is convenient to express the angular distribution or differential cross section as a multipole expansion, provided the recoil energy separating the fragments is much larger than the rotational energy of the parent molecule [23; 24]. Cylindrical

symmetry reduces the expansion exclusively in terms of the Legendre polynomials, equation III.6, and in simple half-collision reactions reduces into the well-known dipolar form, equation III.7.

$$\frac{\mathrm{d}\sigma}{\mathrm{d}\Omega} \equiv I(\theta) = \sum_{l=0}^{\infty} a_l P_l(\cos\theta) \tag{III.6}$$

$$I(\theta) \approx \frac{1}{4\pi} \left[P_0(\cos\theta) + \beta\, P_2(\cos\theta) \right] \tag{III.7}$$

In this form, the second term expansion coefficient in equation III.7, referred to as the asymmetry parameter β, determines the relationship between the transition dipole moment $\boldsymbol{\mu}$ of the parent molecule and the electric vector of the photolysis light $\mathbf{E_{diss}}$ in a half-collision process, Figure 13. For example, a dissociative system with a $\beta = 2$ corresponds to a parallel-type transition, $\beta = -1$ for a perpendicular-type transition, and $\beta = 0$ for an isotropic distribution of photofragments.
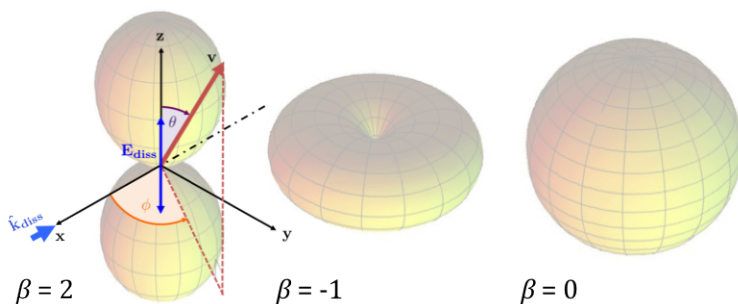

Figure 13. Angular distribution for different photofragmentation processes.

In 1990, Taatjes *et al.* developed a general method for determining cylindrically symmetric velocity distributions using Kinsey's FTDS inversion technique [2]. By employing an expansion in classical orthogonal polynomials (equation III.8), the integral transform in equation III.5 was reduced to a set of purely algebraic relations.

$$D_{cyl}(w; \theta') = \sum_l P_l(\cos \theta') \sum_n a_{l,n} H_n(w) e^{-w^2} \qquad \text{(III.8)}$$

Hermite and Legendre polynomials are arbitrarily elected for integrability, existence, and for their known transform properties [38].

Taatjes *et al.* examined the Doppler profiles of simple molecules undergoing a half-collision process. These profiles exhibit a reflection symmetry about the rest transition frequency, ν_0, reducing the expansion in equation III.8 exclusively to even term polynomials. This argument can be extended to Legendre polynomials, since **1.)** the multipole expansion of the product angular distribution can be truncated to its dipolar form, equation III.7, and **2.)** the linearity of the integral operator enables an analogous expansion for the Doppler profile in terms of w as a function of θ'; see equation III.9. The Taatjes method makes the FTDS inversion computationally robust, simplifying the integral transform into an expression, equation III.10, consisting of expansion coefficients and known functions – i.e. a confluent hypergeometric function and series of gamma functions (Euler integral of the second kind) [2]. Just as in FTDS, a detailed derivation of the Taatjes method, including its expansion coefficients $a_{l,n}$, is provided in Appendix B; note that no derivation of equation III.9 is

provided in either of the referenced articles, in particular [2; 37], nor in Craig Taatjes'

PhD dissertation.

$$F(v, \theta) = 2\pi \int_0^\infty dk\, k^2 \int_0^{2\pi} d\theta' \sin\theta' J_0(2\pi k v \sin\theta' \sin\theta)\, e^{2\pi i (kv)\cos\theta' \cos\theta}$$
$$\cdot \sum_l P_l(\cos\theta') \sum_n a_{l,n} \left[\frac{\sqrt{\pi}}{2}\, i^n\, e^{-\pi^2 k^2} (2\pi k)^n \right]$$

(III.9)

$$F_l(v, \theta) = \frac{v^l\, e^{-v^2}\, P_l(\cos\theta)}{2\pi\, \Gamma\!\left(l + \frac{3}{2}\right)} \sum_n a_{l,n}\, i^{n+l}\, 2^n\, \Gamma\!\left(\frac{3+n+l}{2}\right) {}_1F_1\!\left(\frac{l-n}{2}; l + \frac{3}{2}; v^2\right)$$

(III.10)

3.5   Sample Reconstruction

To test the Taatjes method, equation III.10, we construct a hypothetical velocity

distribution from a one-photon dissociative process that is expressed as the product

of speed- and angle-dependent components, equation III.11.

$$F(v, \theta) = f(v) \cdot I(\theta)$$

(III.11)

$$= \frac{1}{\sqrt{2\pi s^2}}\, e^{-\frac{(v-u)^2}{2s^2}}\, \frac{1}{4\pi} \left[1 + \beta\, P_2(\cos\theta)\right]$$

We plot a parallel-type transition ($\beta = 2$) with an arbitrary Maxwellian speed dis-

tribution in Figure 14, using Mathsoft MathCAD (version 11.1) software. Using the

MathCAD software, the state-selected velocity contour maps are graphed as surface

plots with the x- and y-axes representing indices of an arbitrary range of speed; e.g.

center of the x-y plane on Figure 14 serves as the origin of the polar coordinates v and θ, while the z-axis conveys the likelihood of a particular velocity (i.e. the scattering intensity). The speed distribution in Figure 14 is gaussian with a relative mean speed $u = 2.0$ (equivalent to 761 m/s) and standard deviation $s = 0.2$. The indices in this and subsequent surface plots correspond to a speed range $-v_{max}$ to v_{max}, where $v_{max} = 2u = 1522$ m/s.
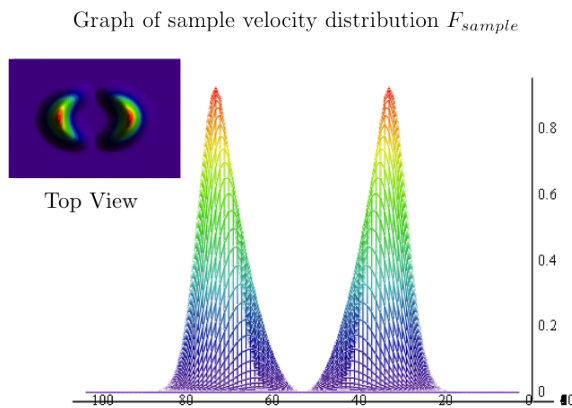
Figure 14. Simulated parallel-type transition using equation III.11. Insert: top view of velocity contour map.

Accounting for the intrinsic symmetry and simplification of the photodissociative process, discussed in Section 3.4, theoretical curves can be derived by means of the Radon transform, equation III.12. A coordinate transformation from (xyz) to (x'y'z') and integration over ϕ'' and θ'' results in the Doppler profile averaged over the distribution $v^2 f(v)$, equation III.13; derived by Schmiedl *et al.* [31]. Doppler profiles of the sample distribution are generated using equation III.13 and fitted with classical

orthogonal polynomials (equation III.8); Figure 15. Fitting the Doppler profiles with the classical orthogonal polynomials in equation III.8 permits reconstruction of the sample distribution from Doppler profiles in Figure 16.

$$D_{cyl}(w;\theta') = \int d^3\mathbf{v}\, F(v,\theta)\, \delta[w - \mathbf{v} \cdot \hat{\mathbf{k}}_{\mathbf{probe}}]$$

$$D_{cyl}(w;\theta') = \int_{v=0}^{\infty} dv\, v^2 \int_{\theta=0}^{\pi} d\theta\, \sin\theta \int_{\phi=0}^{2\pi} d\phi\, f(v)$$

$$\cdot \frac{1}{4\pi}\left[1 + \beta\, P_2(\cos\theta)\right]\delta[w - v\cos\theta''] \tag{III.12}$$

$$D_{cyl}(w;\theta') = \int_{|w|}^{\infty} dv\, v^2\, f(v)\, \frac{1}{2v}\left[1 + \beta\, P_2(\cos\theta')P_2\left(\frac{w}{v}\right)\right] \tag{III.13}$$
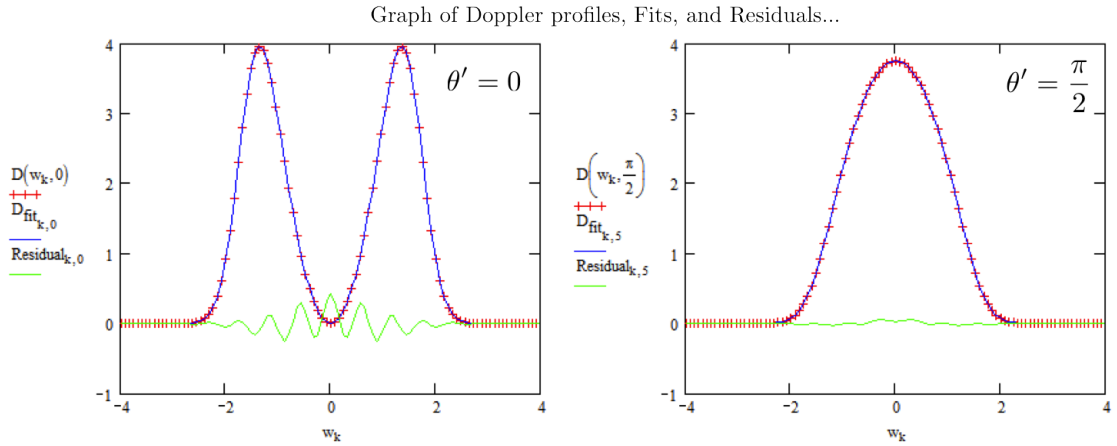

Figure 15. Simulated Doppler profiles using equation III.13. Note: the residual between profile and fit, shown in green, is amplified by 100 fold

Graph of calculated velocity distribution F_{calc}
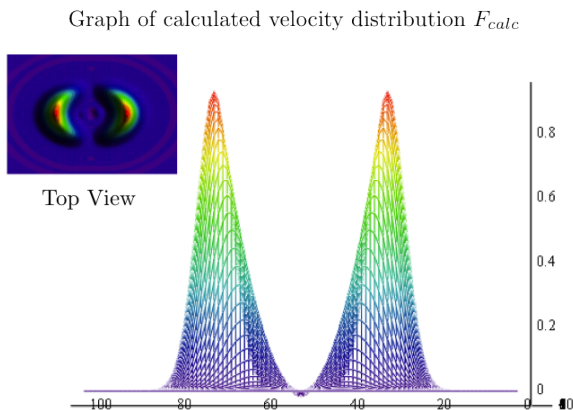
Top View

Figure 16. Velocity distribution recovery using Taatjes method, equation III.10. Insert: top view of velocity contour map.

With successful recovery of the simulated velocity distribution using the Taatjes method, we wanted to test this procedure on asymmetric distributions; e.g. those stemming from full bimolecular collisions. Equation III.10 considers only an even-term expansion in Hermite and Legendre polynomials and results in the symmetry observed about $w = 0$, i.e. the rest transition frequency ν_0; Figure 15. In our bimolecular scattering experiments, we cannot assume the spectral symmetry afforded by half-collision processes; the dynamics from one chemical transformation to another can be very different and can give rise to a distinct anisotropy. Therefore, the incorporation of odd Hermite and Legendre terms of the expansion is necessary to account for the potential asymmetry in the Doppler profiles of asymmetric velocity distributions. Therefore, the derivation from equation III.8 through equation III.10 needed adjustment for our general use with no presumptions of symmetry regarding the profiles. We find a new expression, equation III.15, which incorporates both odd

and even Hermite and Legendre terms and accounts for potential asymmetries in Doppler profiles.

$$F(v,\theta) = 2\pi \int_0^\infty dk\, k^2 \int_0^{2\pi} d\theta'\, \sin\theta'\, J_0(2\pi k v \sin\theta' \sin\theta)\, e^{2\pi i (kv)\cos\theta' \cos\theta}$$

$$\cdot \sum_l P_l(\cos\theta') \sum_n a_{l,n} \left[\sqrt{\pi}\, (-i)^n\, e^{-\pi^2 k^2} (2\pi k)^n \right] \tag{III.14}$$

$$F_l(v,\theta) = \frac{i^l\, v^l\, e^{-v^2}\, P_l(\cos\theta)}{\pi\, \Gamma\!\left(l + \frac{3}{2}\right)} \sum_n a_{l,n}\, (-i)^n\, 2^n\, \Gamma\!\left(\frac{3+n+l}{2}\right) {}_1F_1\!\left(\frac{l-n}{2}; l + \frac{3}{2}; v^2\right) \tag{III.15}$$

The differences between equations III.10 and III.15 are subtle and include a factor of 2 and $(-i)^n$; our derivation of the general method can be found in Appendix B. With these adjustments we were able to recover the same simulated velocity distribution constructed using equation III.11, Figure 17.
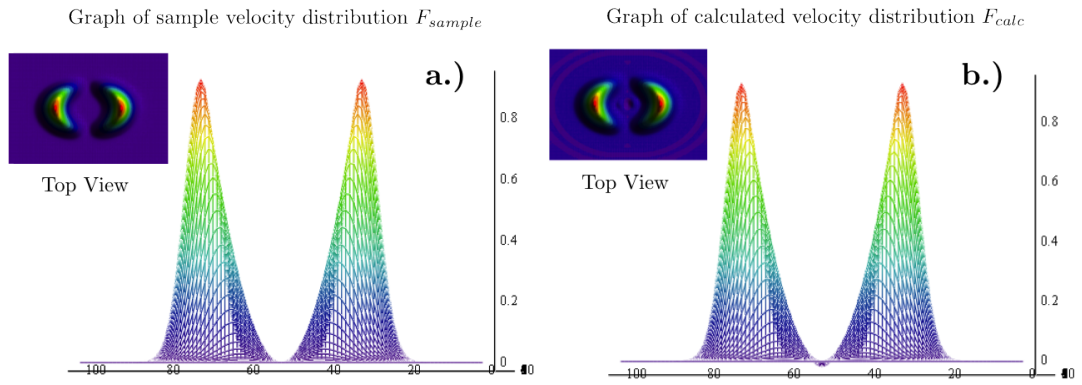
Figure 17. Simulated velocity contour maps parallel-type transitions. **a.)** the simulated velocity distribution and **b.)** the velocity distribtution recovered using equation III.15.

CHAPTER IV

RECONSTRUCTION OF THE ASYMMETRIC DISTRIBUTION

The same mechanism formulated in Section 3.5 was necessary in order to test the utility of the general method, equation III.15, for asymmetric velocity distributions. This procedure involved constructing a sample distribution, mapping the distribution into Radon space, fitting the generated Doppler profiles with even and odd termed Hermite and Legendre polynomials, and recovering the distribution via equation III.15. We chose to simulate the elastic scattering in Argon–Argon collisions primarily for its simplicity and wealth of available data (i.e. cross sections, angular distributions, etc.) at well-defined energies [39–44]. The initial goal of this exercise was to construct the angular distribution from the elastic Argon–Argon interaction (i.e. a forward-scattered distribution) and compute its integral cross section for comparison with an empirically derived cross section.

4.1 The Forward Problem in Scattering: Direct Calculation of the Differential Cross Section

Consider an adiabatic collision between two structureless particles, i and j with mass m_i and m_j, each exerting a force which depends solely on the distance between them, i.e. a conservative system. Provided no external forces or additional energy, the system's Hamiltonian can be expressed as a function of kinetic energy, T, and potential energy, V. If the kinetic energy of the system is a homogeneous quadratic

function of velocity, the Hamiltonian is equivalent to the total mechanical energy of the system, E_{total}, equation IV.1.

$$H = T(|\dot{\mathbf{r}}|) + V(r) = E_{total} \tag{IV.1}$$

$$T(\dot{r}, \dot{\psi}, \dot{\phi}) = \frac{1}{2}\mu\left(\dot{r}^2 + r^2\dot{\psi}^2 + r^2\sin^2\psi\,\dot{\phi}\right)$$

The scattering produced between two colliding bodies is constrained by the total mechanical energy of the system, a constant of motion. This constrain defines the collision border on the reaction's Newton (velocity) sphere; a spherical frame with spherical frame with one body fixed at the center (the so-called "target") and another approaching in a straight line, Figure 18.

For structureless particles the collision products are constrained to lie on a "plane" formed by the impact parameter b and the velocity of the incident-body v; a direct result of angular momentum conservation. Furthermore, rotation of the impact parameter about the target-body axis, i.e. the incident trajectory at $b = 0$, traces a set of incident-body trajectories that give rise to an isotropy about the azimuthal angle ϕ, referred to as cylindrical symmetry; the bullseye or dartboard picture in Figure 18. As the impact parameter between two colliding bodies increases, the probability of observing the reaction generally decreases. This probability is conveyed by the area swept out by the largest impact parameter b_{max} (that still causes an observable reaction) and is referred to as the effective cross section, $\sigma(b, E_{total})$.
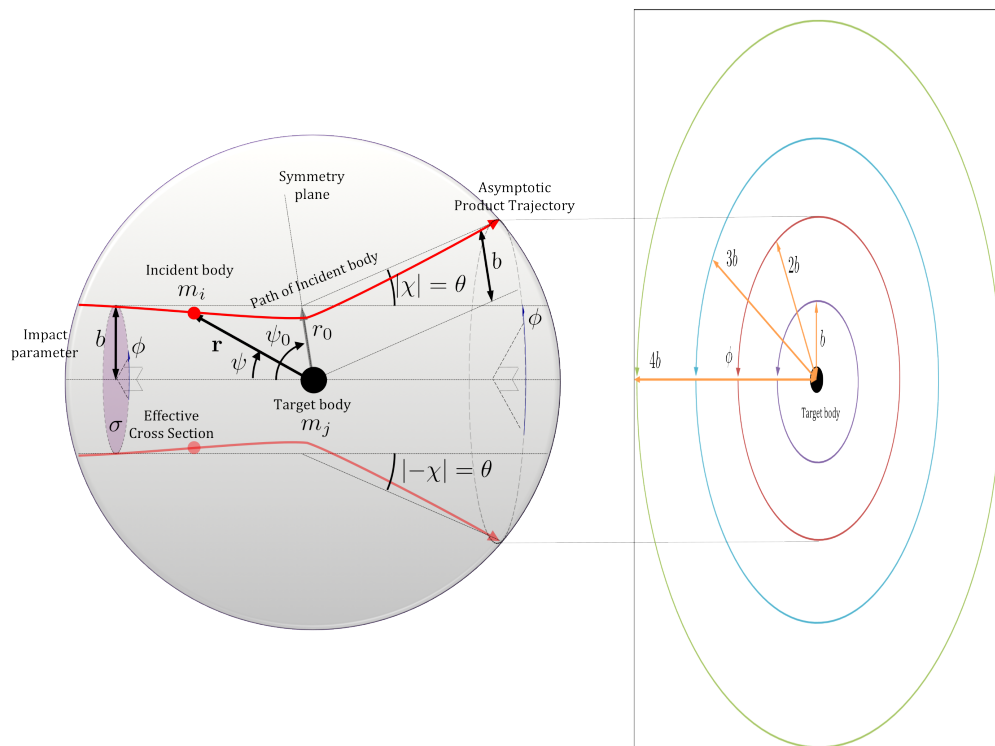
Figure 18. Classical scattering process.

Scattering trajectories are unique to the velocity v and impact parameter b in an adiabatic/elastic collision. To discern the underlying dynamics of of a reaction, we observe the scattering product trajectories in the form of a deflection angle distribution, better known as the differential cross section. The differential cross section one would observe for an adiabatic collision between two closed-shell Argon atoms can be constructed from a spherically symmetric intermolecular potential; the so-called forward problem in scattering. The functional form of this central potential is arbitrary and examples can be found in Hirschfelder *et al.* [45]. We opt for the Lennard-Jones 6-12 potential function, equation IV.2, for its simplicity and its extensive use in de-

scribing the Ar + Ar system [39; 41; 44].

$$V(r) = 4\epsilon \left[\left(\frac{\sigma}{r} \right)^{12} - \left(\frac{\sigma}{r} \right)^{6} \right] \qquad \text{(IV.2)}$$

Deflection via a Repulsive Barrier

The Lennard-Jones 6-12 potential function gives a fairly simple and realistic representation for spherical non-polar molecules. The potential is non-monotonic, Figure 19, with the $-r^{-6}$ representing the induced-dipole-induced-dipole interaction at long range (i.e. the attractive term) and r^{-12} approximating the repulsive contribution; whose index is a result of mathematical convenience and is by no means unique. The parameters ϵ and σ correspond to the maximum energy of attraction (i.e. depth of potential well) and the value of r for which $V(r) = 0$, respectively. Figure 19 is an example plot of the LJ 6-12 potential, along with its components, for an Argon– Argon interaction with parameters σ and ϵ equal to 3.40 Å and 141.3 K, respectively. These values were obtained from Kalos *et al.* for a 369.0 Å^{2} collision cross section at 60 *m*eV [39].
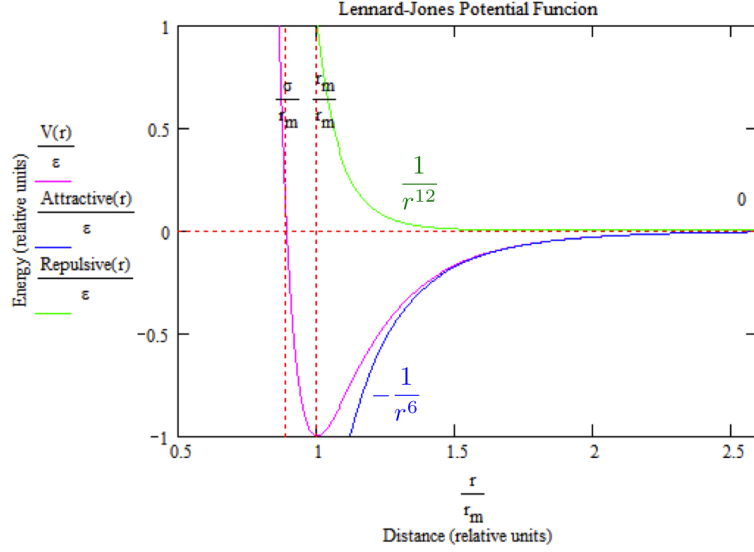
Figure 19. Lennard-Jones 6-12 potential function and its components.

Deflection of the incident-body as it approaches the target is caused by the repulsive nature of the potential and the centrifugal barrier; the perceived repulsive force derived from the angular motion of the system. Together, these repulsive components of the interaction are known as the effective potential, $U_{eff}(r,b)$, equation IV.3.

$$U_{eff}(r,b) = \frac{1}{2}\mu\, r^2 \dot{\psi}^2 + V(r)$$

$$= E_{total}\frac{b^2}{r^2} + V(r) \qquad (IV.3)$$

Considering the symmetry of the collision and grouping centrifugal and potential energy terms into an "effective potential" simplifies equation IV.1 from three coordinates into one, equation IV.4. Figure 20 is a plot of the effective potential at $b=0$, $\frac{1}{2}r_m$,

36

r_m, and $\frac{3}{2}$ from an Argon–Argon collision from a collision with a $E_{total} = 5\,\epsilon$; equivalent to a relative velocity $\dot{r} = 761$ m/s.

$$E_{total} = \frac{1}{2}\mu\left(\dot{r}^2 + r^2\dot{\psi}^2\right) + V(r)$$

$$= \frac{1}{2}\mu\dot{r}^2 + E_{Total}\frac{b^2}{r^2} + V(r) \tag{IV.4}$$

$$= T_{rel}(\dot{r}) + U_{eff}(r, b)$$
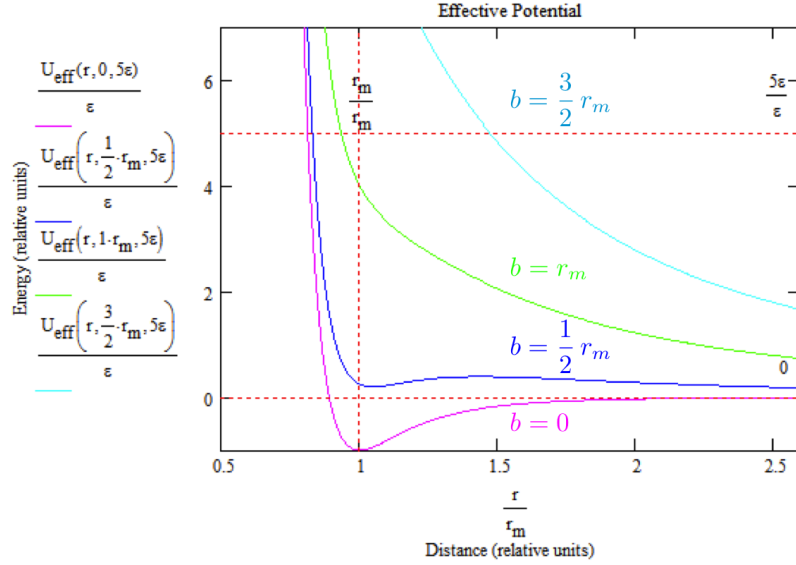
Figure 20. Effective potential at $E_{total} = 5\,\epsilon$ with varying impact parameter.

By expressing the change in ψ in terms of the change in r, we can obtain the apsidal angle ψ_0, the angular span between the direction where a minimum and maximum r are obtained, equation IV.5. The trajectory of the incident-body is hyperbolic (i.e. an open orbit) with apsides at $r_{min} = r_0$ and $r_{max} = \infty$, where r_0 corresponds to the

distance of closest approach. The trajectory of the incident-body is hyperbolic (i.e. an open orbit) with apsides at $r_{min} = r_0$ and $r_{max} = \infty$, where r_0 corresponds to the distance of closest approach.

$$\psi_0 = \int_{r_0}^{\infty} \mathrm{d}r \, \frac{\dot{\psi}}{\dot{r}}$$

$$= b \int_{r_0}^{\infty} \mathrm{d}r \, \frac{1}{r^2 \sqrt{1 - \frac{U_{eff}(r,b)}{E_{total}}}} \tag{IV.5}$$

ψ_0 defines a line of symmetry for the trajectory with impact parameter b, Figure 18. From this symmetry, the deflection angle χ can be obtained, equation IV.6.

$$\chi(b) = \pi - 2 \, b \, \psi_0 \tag{IV.6}$$

$$= \pi - 2b \int_{r_0}^{\infty} \mathrm{d}r \, \frac{1}{r^2 \sqrt{1 - \frac{U_{eff}(r,b)}{E_{total}}}}$$

Due to the inherent symmetry observed in collisions between structureless particles, i.e. the cylindrical symmetry about $b = 0$, the sign of the deflection angle χ is not experimentally meaningful; some deflection angles within a range b to $b + \mathrm{d}b$ are indistinguishable from its negative counterpart -[b to $b + \mathrm{d}b$]. Therefore, the "observable" deflection angle θ corresponds to the absolute value of the computed deflection angle χ, i.e. $\theta(b) = |\chi(b)|$; Figure 21. Computing the apsidal angle and subsequent deflection angles χ and θ are E_{total}-dependent calculations, as seen in equations IV.5 and IV.6. Figure 21 was computed for a $E_{total} = 5 \, \epsilon$ equivalent to a relative velocity

$\dot{r} = 761$ m/s.
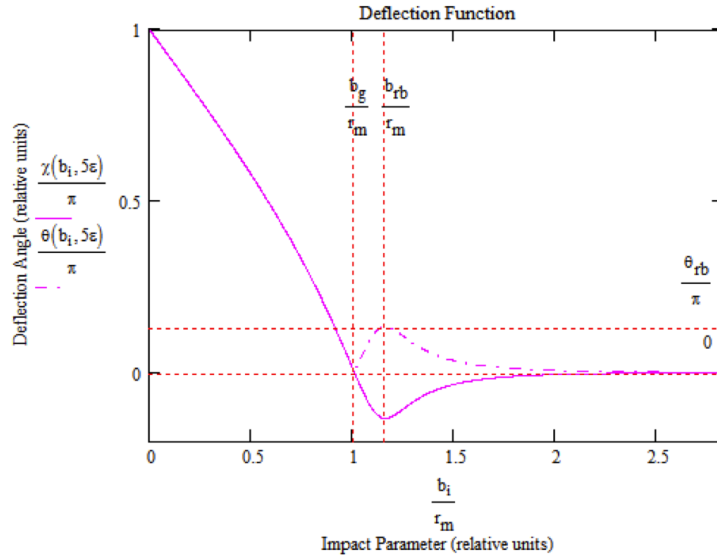
Figure 21. Deflection angles χ and θ at $E_{total} = 5\,\epsilon$.

The Differential and Integral Cross Sections

The differential cross section of a reaction is the flux of products undergoing a deflection into a range θ to $\theta + \mathrm{d}\theta$; i.e. the change in reaction cross section with change in solid angle, $\mathrm{d}\Omega$. The differential cross section of a cylindrically symmetric collision can be computed using equation IV.7 and is a E_{total}-dependent calculation.

$$\frac{\mathrm{d}\sigma}{\mathrm{d}\Omega} \equiv I(\theta) = \frac{2\pi\,b\,\mathrm{d}b}{2\pi\,\sin\theta\,\mathrm{d}\theta} = \frac{b}{\sin\theta\left(\frac{\mathrm{d}\theta}{\mathrm{d}b}\right)}$$

$$= \frac{b}{\sin\theta\left|\frac{\mathrm{d}\chi}{\mathrm{d}b}\right|} \qquad\qquad \text{(IV.7)}$$

39

Figure 22 provides a plot of the scattering intensity (logarithmic scale) with varying deflection angle θ at $E_{total} = 5\,\epsilon$.
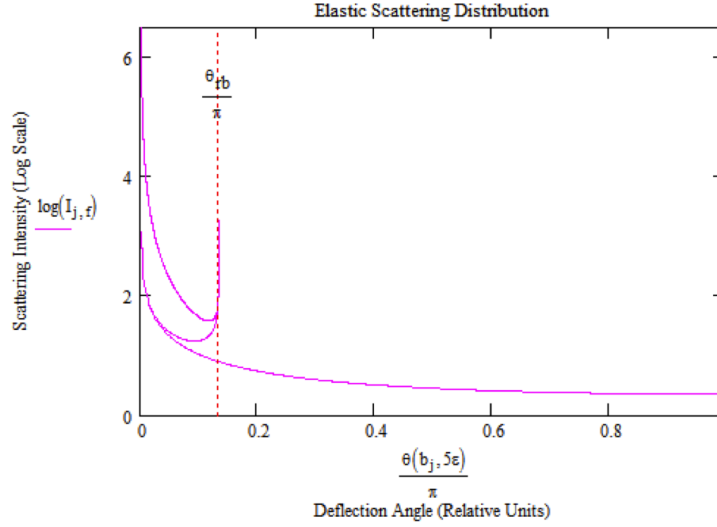
Figure 22. Angular distribution at $E_{total} = 5\,\epsilon$ for elastic scattering in Ar–Ar.

From Figure 21 it is evident a one-to-one correspondence does not exist between impact parameter b and the deflection angle θ. This phenomenon gives rise to the three curves present in the angular distribution plot, Figure 22; each corresponding to range of impact parameters defined by the singularities at $\theta = 0$ and the rainbow angle $\theta_{rb} \equiv \frac{d\theta}{db} = 0$. To obtain a one-to-one correspondence, between the scattering intensity $I(\theta)$ and θ, the three curves must be summed for all $\theta \leq \theta_{rb}$, equation IV.8.

$$I(\theta) = \sum_{i=1}^{3} \frac{b_i}{\sin\theta \left| \frac{d\chi}{db} \right|_{b=b_i}} \tag{IV.8}$$

40

In addition to this summation, we choose to ignore the singularities at $\theta = 0$ and θ_{rb} by rounding their scattering intensities. This was done (initially) by selecting an arbitrary Δb that effectively steps over these values and fitting that distribution via a cubic spline fit, Figure 23.
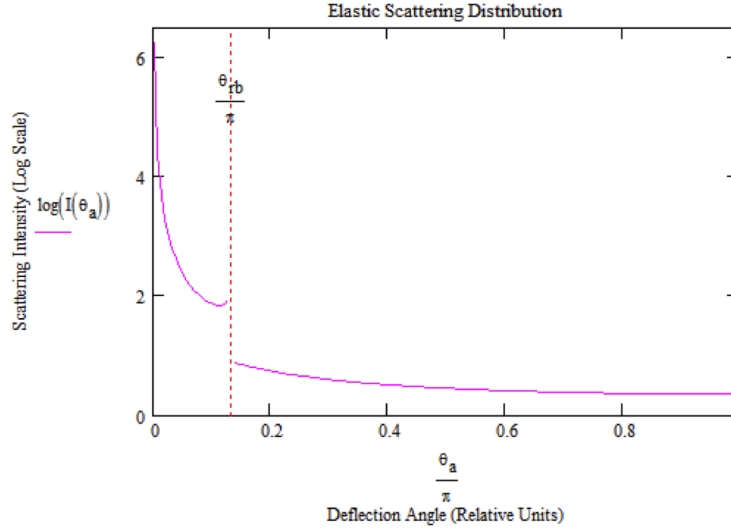
Figure 23. Cubic spline fit of angular distribution at $E_{total} = 5\,\epsilon$.

Integration of the differential cross section over the entire solid angle yields the integral/total cross section of the reaction, equation IV.9.

$$\sigma(\theta, E_{total}) = \int_\Omega d\Omega \, \frac{d\sigma}{d\Omega} = 2\pi \int_{\theta_{min}}^{\pi} d\theta \, I(\theta, E_{total}) \sin\theta \qquad \text{(IV.9)}$$

$$\implies \quad \theta_{min} = \frac{\left(4\,\epsilon\,\sigma^6\right)}{\left(b_{max}\right)^6 T_{rel}}$$

$$\sigma(b, E_{total}) = 2\pi \int_0^{b_{max}} db\,b \qquad \text{(IV.10)}$$

41

Initial attempts to compute the integral cross section resulted in a larger than expected value. We attributed this result to the large Δb used to construct the angular distribution, which lead to an inadequate spline fit about $I(\theta_{min})$. We implemented an arbitrary rounding scheme, equation IV.11 that produced a smooth curve about $I(\theta_{min})$ resulting in a finite value for $I(\theta = 0)$; c is the index number used in our spline fit, where the total number of points used was 3000.

$$I(\theta_c \leq \theta_4) = I(\theta_4)\left[\frac{7 - c}{2}\right]^{\frac{1}{2}} \tag{IV.11}$$

With these modifications to equation IV.8, we calculated a $\sigma = 367.6$ Å^2, in close agreement with $\sigma = 369.0$ Å^2 Kalos *et al.*.

4.2 Mapping the Distribution in Radon Space

The simulated velocity distribution was separable into speed- and angle-components. The choice of speed distribution is arbitrary and we choose a Maxwellian distribution about the relative speed of our collision; i.e. $\dot{r} = 761$ m/s with a relative standard deviation $s = 0.2$. Using equation III.11 and our calculated angular distribution we obtain Figure 24. In order to map the distribution in Radon space, we applied equation III.13 to our hypothetical velocity distribution in photodissociation. Equation III.13 provides an N to N correspondence between $F(v, \theta)$ and $D(w; \theta')$, but specifically for an angular distribution with two moments (monopole and dipole terms). For our general reconstruction efforts, equation III.15 requires a multipole expansion of the angular distribution. We modified equation III.13 for a general ex-

pansion in Legendre polynomials; equation IV.12.

$$D_{cyl}(w; \theta') = \int_{|w|}^{\infty} dv \, v^2 \, f(v) \, \frac{1}{2v} \left[\sum_{l=0}^{\infty} a_l \, P_l(\cos \theta') P_l \left(\frac{w}{v} \right) \right] \quad \text{(IV.12)}$$
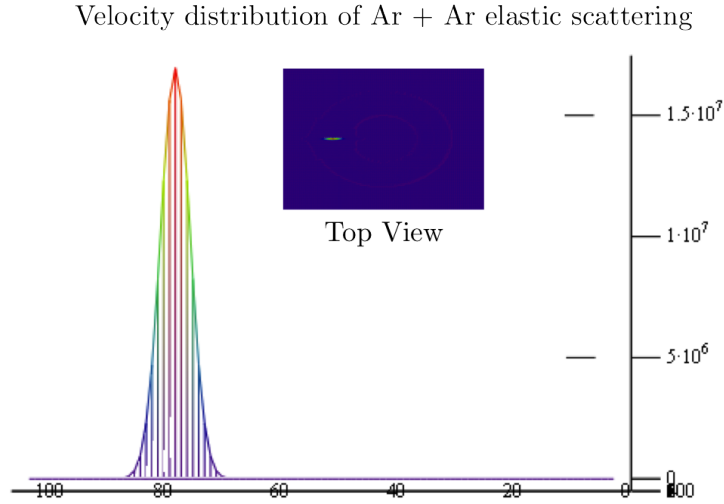
Figure 24. Velocity contour map of Ar–Ar elastic scattering at $E_{total} = 5\,\epsilon$. Insert: top view of velocity contour map.

Our initial fits of the angular distribution were unsatisfactory resulting in the large oscillations observed in Figure 25a, even with an expansion of 500 Legendre terms.

Attributed to the high-order Legendre terms, these high-frequency oscillations are necessary to mimic the sharp features present in our angular distribution about $\theta = 0$ and θ_{rb}. In order to fit the distribution properly, further modification or smoothing of these sharp features are required unless a significant number of additional Legendre terms are used for the polynomial fit, as in Figure 25b; the later is computationally

expensive and time consuming for a single computer processor running MathCAD.
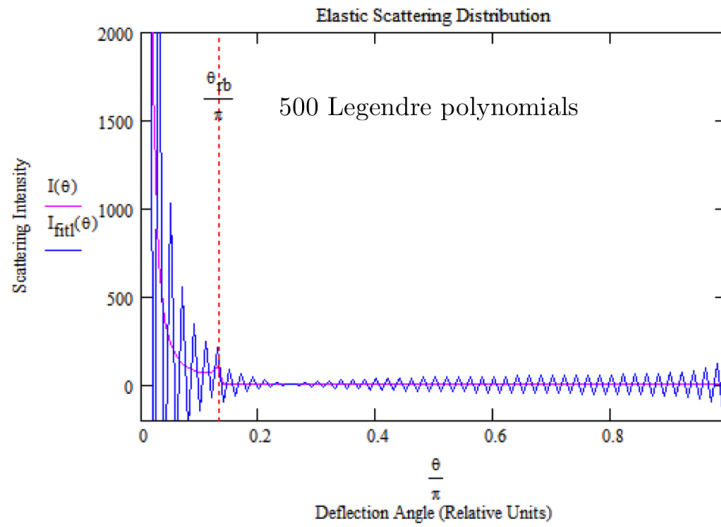
(a) Fit of angular distribution with 500 Legendre terms
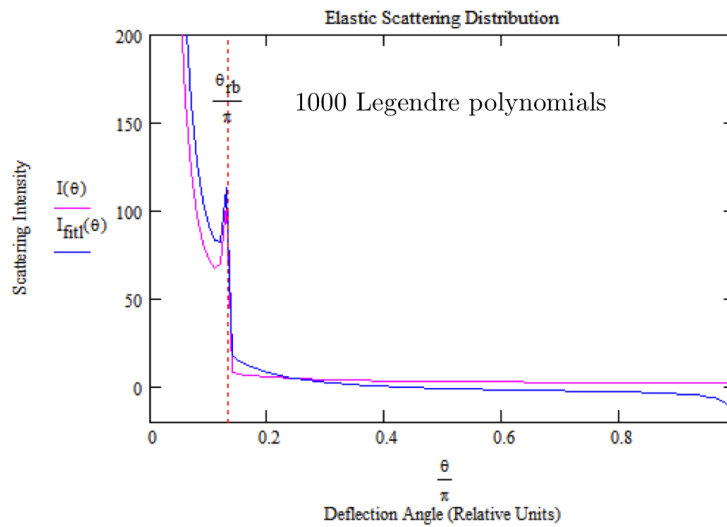
(b) Fit of angular distribution with 1000 Legendre terms

Figure 25. Multipole expansion of the angular distribution.

To compute the large number of expansion terms necessary to properly fit the acquired Doppler profiles, multiple processors are needed to run the calculation. We recognize the sharp features in this simulated angular distribution are not observed experimentally, but are artifacts of a classical formulation in scattering. What is observed at $\theta = 0$ and θ_{rb} are finite-smooth features due to quantum resonances [3]. The sharp features in the distribution in our classically derived distribution was smoothed via an expansion in Jacobi polynomials, equation IV.13, providing a smooth curve (parameters at $\alpha = 3.5$ and $\beta = 0$) that crudely mimicked the shape of the original distribution with 30 expansion terms.

Orthogonality of Jacobi Polynomials

$$\int_0^\infty \mathrm{d}\theta\, P_m^{(\alpha,\beta)}(\cos\theta) P_n^{(\alpha,\beta)}(\cos\theta)\,(1-\cos\theta)^\alpha(1-\cos\theta)^\beta$$
$$= \frac{2^{\alpha+\beta+1}}{2n+\alpha+\beta+1}\,\frac{\Gamma(n+\alpha+1)\,\Gamma(n+\beta+1)}{n!\,\Gamma(n+\alpha+\beta+1)}\,\delta_{m,n} \tag{IV.13}$$

This fit allowed for another expansion in Legendre polynomials, Figure 26, and for the generation of Doppler profiles via equation IV.12.
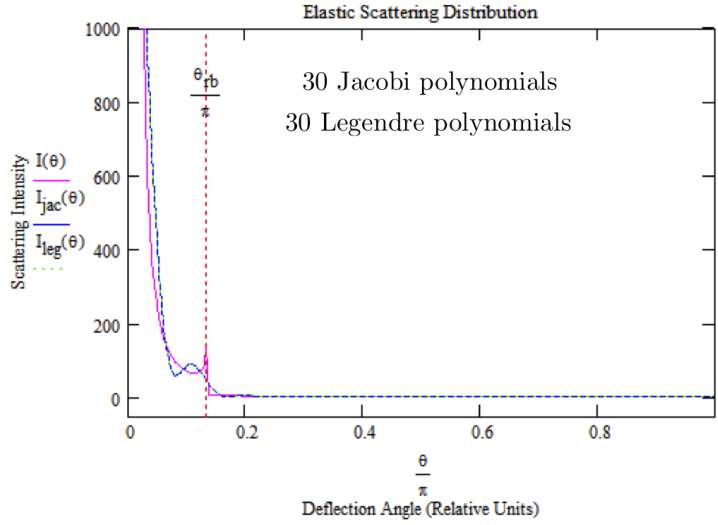
Figure 26. Angular distribution fit with Jacobi and Legendre polynomials. The blue line represents the Jacobi fit, while the green line represents the Legendre fit.

The crude fit with 30 Legendre polynomials, in Figure 26, resulted in an integral cross section $\sigma = 152.5$ Å^2. An incorrect integral cross section was expected from this crude fit due to the low intensities near $\theta = 0$, but the behavior/shape of the curve was much like those observed in Kalos *et al.*, Cavallini *et al.*, and Lee *et al.*; [39; 41; 43]. Using our arbitrary Maxwellian speed distribution, we can generate a contour map of our separable velocity distribution, Figure 27a.

Velocity distribution from Jacobi Fit Curve
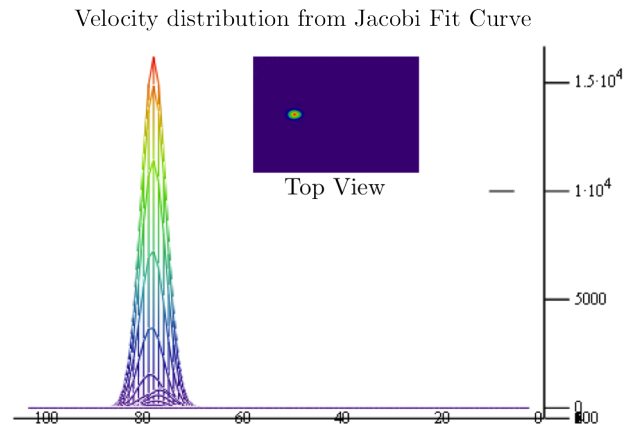
(a) Velocity contour map of simulated velocity distribution.

Doppler profiles of sample velocity distribution
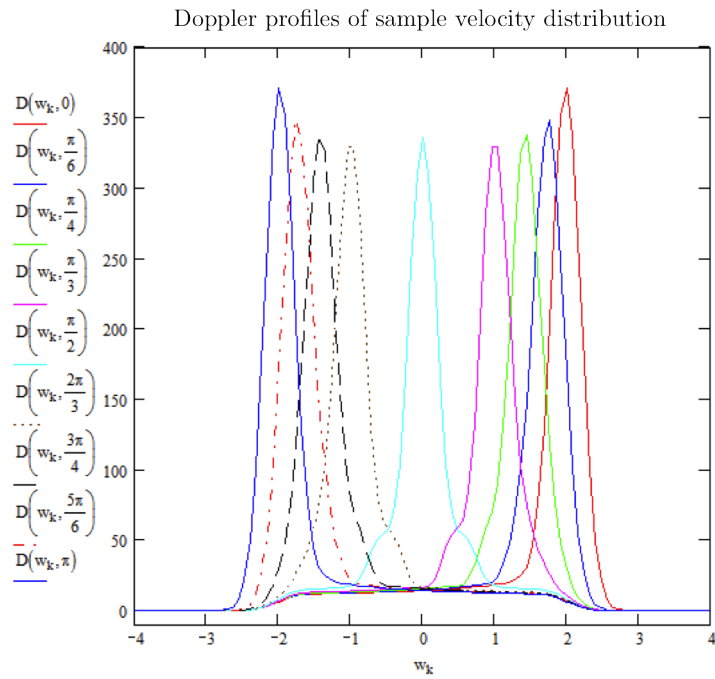
(b) Doppler profiles of the simulated velocity distribution.

Figure 27. Velocity contour map and Doppler profiles of Jacobi fit curve.

4.3 Reconstruction of the Distribution via FTDS

Mapping the distribution in Figure 27a into Radon space using equation IV.12 produces the Doppler profiles generated in Figure 27b. We generated 100 discrete Doppler profiles at unique angles in an attempt to reconstruct the simulated distribution in Figure 27a. The resolution of each Doppler profile consisted of 100 data points, equivalent to our data collection scheme; detuning our microwave source in increments of 0.02 MHz over a range of 2.00 MHz. The generated lineshapes are fitted with 50 Hermite and 50 Legendre terms (includes even and odd expansion terms) with simulated profiles, fits, and residuals plotted in Figure 28a. It is evident from residuals plots in Figure 28a that the fit was inadequate.
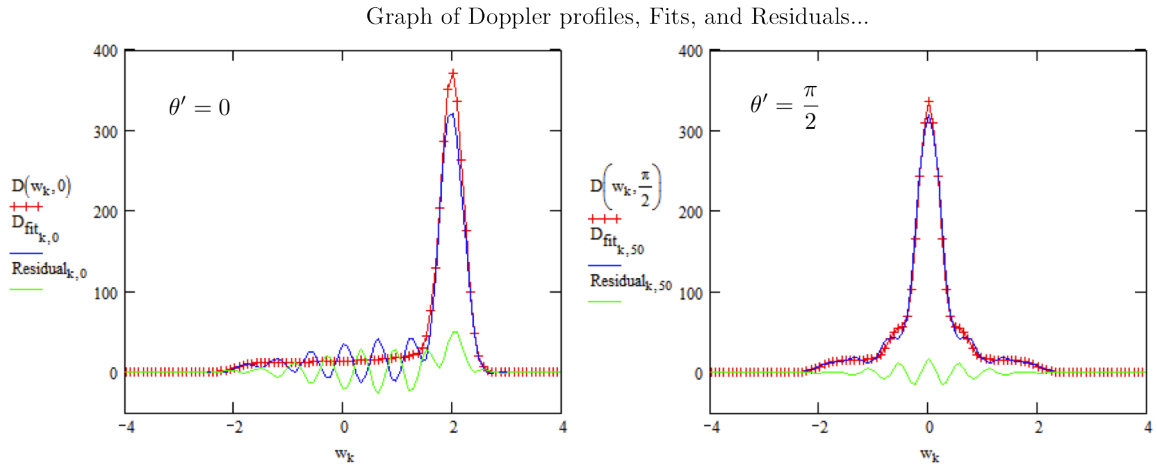
(a) Fit of simulated Doppler profile with Hermite and Legendre polynomials.
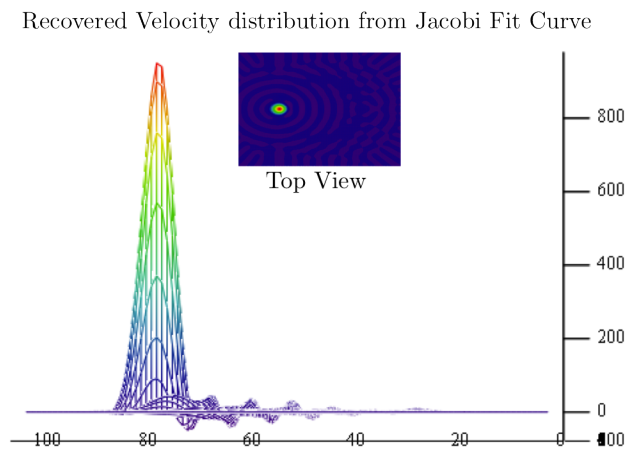
(b) Velocity contour map of distribution recovered from Doppler profiles in Figure 28a.

Figure 28. Fit of Doppler profiles and FTDS recovered velocity contour map.

In an effort to demonstrate the caution and detail necessary to properly construct a velocity distribution using the FTDS inversion procedure, we attempted to reconstruct the distribution from these Doppler fits. The expansion coefficients, derived from the fit above, and our analytical expression for FTDS, equation III.15, produce

the velocity distribution in Figure 28b.

The inability of the method to recover the exact distribution in Figure 27a is attributed to the resolution of the simulated Doppler profiles. Again, 100 discrete Doppler profiles were generated with a $\Delta\theta' = \frac{\pi}{30}$ between each one. These large steps in θ' do not provide enough points to properly fit the higher order expansion terms, as seen in by the high frequency oscillations in Figure 28a. A smaller $\Delta\theta'$ and Δw would provide more data points to properly fit the higher order polynomial terms. This observation confirms a suspicion we had regarding our experimental set-up; in order to properly reconstruct an observable distribution, we would need high angular resolution for θ'. Our current set-up at best provides a one degree resolution assuming little to no angular divergence from our molecular beam(s). The high resolution scans would require Doppler scans with smaller frequency steps (e.g. 200 steps spanning 2 MHz) at each accessible angle. Fitting the Doppler profiles with more Hermite and Legendre polynomials would also produce better fits of the velocity distribution and eliminate the unwanted contributions from higher order terms.

CHAPTER V

CONCLUSION

In this investigation, we report an extension of the Taatjes *et al.* general method for reconstructing cylindrically symmetric velocity distributions. The modifications allow for the tomographic reconstruction of asymmetric velocity distributions found in crossed-molecular beam experiments. To test the method, we chose to construct a sample asymmetric distribution from classical elastic scattering in the Argon–Argon collision system. The choice of the well-studied Argon–Argon was arbitrary and primarily considered for its simplicity. Doppler profiles were generated using a method developed by Schmiedl *et al.* and fit using classical orthogonal polynomials. Recovering the exact distribution in this collision system was of limited success due the sharp features in the calculated distribution, the angular resolution used in our reconstruction procedure, and the insufficient number of expansion terms used to fit the generated Doppler profiles.

In hindsight, a quantum constructed angular distribution from elastic Argon–Argon collisions would have produced a smoother curve for reconstruction, via the FTDS inversion procedure, than the idealized curve we calculated classically. A reactive scattering potential with broader features should be investigated before applying FTDS and our general method of recovery to laboratory acquired data. A prime system to investigate would be the well-studied $H_2 + F$ reaction. An expan-

sion in Legendre polynomials for the center-of-mass angular distribution data in this reaction, e.g. in Neumark *et al.*, should be obtained to properly fit the generated profiles with equation IV.12. This scheme provides the appropriate number of terms in equation IV.12 and the Doppler fits in equation III.8. Such a study would test the feasibility of FTDS and our general method in reconstructing velocity distributions from acquired Doppler profiles.

REFERENCES

[1] J. L. Kinsey, "Fourier transform doppler spectroscopy: A new means of obtaining velocity-angle distributions in scattering experiments," *J. Chem. Phys.*, vol. 66, no. 6, pp. 2560–2565, 1977.

[2] C. A. Taatjes, J. I. Cline, and S. R. Leone, "A general method for doppler determination of cylindrically symmetric velocity distributions: An application of fourier transform doppler spectroscopy," *J. Chem. Phys.*, vol. 93, no. 9, pp. 6554–6559, 1990.

[3] R. D. Levine, *Molecular Reaction Dynamics*. New York, NY: Cambridge University Press, 2005.

[4] D. R. Herschbach, "Molecular dynamics of elementary chemical reactions (Nobel Lecture)," *Angew. Chem. Int. Ed. Engl.*, vol. 26, no. 12, pp. 1221–1243, 1987.

[5] D. M. Neumark, A. M. Wodtke, G. N. Robinson, C. C. Hayden, K. Shobatake, R. K. Sparks, T. P. Schafer, and Y. T. Lee, "Molecular beam studies of the $F + D_2$ and $F + HD$ reactions," *J. Chem. Phys.*, vol. 82, no. 7, pp. 3067–3077, 1985.

[6] X. Yang, "State-to-state dynamics of elementary bimolecular reactions," *Annual Review of Physical Chemistry*, vol. 58, no. 1, pp. 433–459, 2007.

[7] A. G. Suits and Y. T. Lee, *Springer Handbook of Atomic, Molecular, and Optical Physics*, ch. "Reactive Scattering", pp. 967–982. New York, NY: Springer-Verlag, 2nd ed., 2007.

[8] H. Pauly and J. P. Toennies, "The study of intermolecular potentials with molecular beams at thermal energies," in *Advances in Atomic and Molecular Physics* (D. Bates and I. Estermann, eds.), vol. 1, pp. 195–344, Academic Press, 1965.

[9] R. Campargue, "Historical Account And Branching To Rarefied Gas Dynamics Of Atomic and Molecular Beams : A Continuing And Fascinating Odyssey Commemorated By Nobel Prizes Awarded To 23 Laureates In Physics And Chemistry," *AIP Conf. Proc.*, vol. 762, no. 1, pp. 32–46, 2005.

[10] H. Goldstein, *Classical Mechanics*. Addison-Wesley series in physics, Reading, MA: Addison-Wesley Publishing Company, Inc, 2nd ed., 1980.

[11] V. Engel, *Springer Handbook of Atomic, Molecular, and Optical Physics*, ch. "Time-Resolved Molecular Dynamics", pp. 547–553. New York, NY: Springer-Verlag, 2$^{\text{nd}}$ ed., 2007.

[12] P. Y. Cheng, J. S. Baskin, and A. H. Zewail, "Dynamics of clusters: From elementary to biological structures," *PNAS*, vol. 103, no. 28, pp. 10570–10576, 2006.

[13] G. Roberts, "Femtosecond chemical reactions," *Phil. Trans. R. Soc. Lond. A*, vol. 358, no. 1766, pp. 345–366, 2000.

[14] D. R. Miller, *Atomic and molecular beam methods*, vol. 1, ch. "Free Jet Sources", pp. 14–53. New York, NY: Oxford University Press, 1988.

[15] D. H. Levy, "The spectroscopy of very cold gases," *Science*, vol. 214, no. 4518, pp. 263–269, 1981.

[16] S. Y. T. van de Meerakker, H. L. Bethlem, and G. Meijer, "Taming molecular beams," *Nat. Phys.*, vol. 4, pp. 595–602, 08 2008.

[17] A. Tarantola, *Inverse Problem Theory And Methods For Model Parameter Estimation.* Philadephia, PA: Society for Industrial and Applied Mathematics, 2005.

[18] N. H. T. Lemes, E. Borges, R. V. Sousa, and J. P. Braga, "Potential energy function from differential cross-section data: An inverse quantum scattering theory approach," *Int. J. Quantum Chem.*, vol. 108, no. 13, pp. 2623–2627, 2008.

[19] N. R. Mark, D. T. Mauney, J. R. Monge, and L. M. Duffy, "A new crossed-molecular beam instrument, with an eye towards sub-kelvin studies," in 23$^{\text{rd}}$ *Dynamics of Molecular Collisions Conference*, (Snow- bird, UT), July 2011.

[20] L. M. Duffy, "Photodissociation dynamics in "hyper-rovibronic" detail: Exploring the potential of millimeter/submillimeter-wave spectroscopy in molecular reaction dynamics experiments," *Rev. Sci. Instrum.*, vol. 76, no. 9, pp. 093104–093111, 2005.

[21] J. M. Mestdagh, J. P. Visticot, and A. G. Suits, "Doppler spectroscopy, a powerful tool for studying molecular collision dynamics," in *Laser Techniques for State-Selected and State-to-State Chemistry II* (J. W. Hepburn, ed.), vol. 2124, pp. 48–57, SPIE, 1994.

[22] E. J. Murphy, *Laser Induced Fluorescence as a Probe of Detailed Reaction Dynamics: Conventional Techniques and Fourier Transform Doppler Spectroscopy.* PhD thesis, Massachusetts Institute of Technology, Department of Chemistry, 1980.

[23] R. N. Zare and D. R. Herschbach, "Doppler line shape of atomic fluorescence excited by molecular photodissociation," *Proc. IEEE*, vol. 51, no. 1, pp. 173–182, 1963.

[24] R. N. Zare, "Photoejection Dynamics," *Mol. Photochem.*, vol. 4, pp. 1–37, 1972.

[25] H. Meyer, *Atomic and Molecular Beams: The State of the Art 2000*, ch. "Counterpropagating Pulsed Molecular Beam Scattering", pp. 497–518. Physics and Astronomy Online Library, New York, NY: Springer-Verlag, 2001.

[26] S. R. Deans, *The Transforms and Applications Handbook*, ch. "Radon and Abel Transforms", pp. 8.1–8.51. Boca Raton, FL: CRC Press, 2nd ed., 2000.

[27] A. L. Balandin, N. G. Preobrazhenskii, and A. I. Sedel'nikov, "Tomographic determination of particle distribution by velocities," *J. App. Mech. Tech. Phys.*, vol. 30, pp. 862–865, 1989.

[28] R. Piessens, *The Hankel Transform*, pp. 9.1–9.17. Boca Raton, FL: CRC Press, 2nd ed., 2000.

[29] S. W. Smith, *The Scientist and Engineer's Guide to Digital Signal Processing*. San Diego, CA: California Technical Pub., 1st ed., 1997.

[30] E. J. Murphy, J. Brophy, G. S. Arnold, W. L. Dimpfl, and J. L. Kinsey, "Velocity and angular distributions of reactive collisions from fourier transform doppler spectroscopy: First experimental results," *J. Chem. Phys.*, vol. 70, no. 12, pp. 5910–5911, 1979.

[31] R. Schmiedl, H. Dugan, W. Meier, and K. H. Welge, "Laser doppler spectroscopy of atomic hydrogen in the photodissociation of HI," *Z. Phys. A - Atoms and Nuclei*, vol. 304, pp. 137–142, 1982.

[32] M. Dubs, U. Brühlmann, and J. R. Huber, "Sub-doppler laser-induced fluorescence measurements of the velocity distribution and rotational alignment of NO photofragments," *J. Chem. Phys.*, vol. 84, no. 6, pp. 3106–3119, 1986.

[33] A. Ticktin and J. R. Huber, "Fourier transform doppler spectroscopy of the photodissociation of polyatomic molecules: Energy pair correlations and velocity distributions," *Chem. Phys. Lett.*, vol. 156, no. 4, pp. 372–380, 1989.

[34] F. J. Aoiz, M. Brouard, P. A. Enriquez, and R. Sayos, "Analysis of product doppler-broadened profiles generated from photoinitiated bimolecular reactions," *J. Chem. Soc. Faraday Trans.*, vol. 89, pp. 1427–1434, 1993.

[35] M. Brouard, S. Duxon, P. A. Enriquez, and J. P. Simons, "Stereodynamics of photon-induced reactions via doppler-resolved laser-induced fluorescence spectroscopy: Photodissociation of $HONO_2$ and the reaction of O^{1D} with CH_4," *J. Chem. Soc. Faraday Trans.*, vol. 89, pp. 1435–1442, 1993.

[36] S. Klee, K. H. Gericke, and F. J. Comes, "Doppler spectroscopy of OH in the photodissociation of hydrogen peroxide," *J. Chem. Phys.*, vol. 85, no. 1, pp. 40–44, 1986.

[37] J. I. Cline, C. A. Taatjes, and S. R. Leone, "Diode laser probing of $I^*(^2P_{1/2})$ doppler profiles: Time evolution of a fast, anisotropic velocity distribution in a thermal bath," *J. Chem. Phys.*, vol. 93, no. 9, pp. 6543–6553, 1990.

[38] G. Szegö, *Orthogonal Polynomials*. Colloquium Publications - American Mathematical Society, Providence, RI: American Mathematical Society, 4th ed., 1939.

[39] F. Kalos and A. E. Grosser, "Intermolecular potentials from differential cross sections: Ar + Ar," *Canad. J. Chem.*, vol. 50, no. 6, pp. 892–896, 1972.

[40] F. Kalos and A. E. Grosser, "Crossed molecular beam measurement of the N_2 + Ar differential elastic cross section: Energy dependence of the rainbow scattering," *Chem. Phys. Lett.*, vol. 6, no. 5, pp. 537–540, 1970.

[41] M. Cavallini, G. Gallinaro, L. Meneghetti, G. Scoles, and U. Valbusa, "Rainbow scattering and the intermolecular potential of Argon," *Chem. Phys. Lett.*, vol. 7, no. 2, pp. 303–305, 1970.

[42] M. Cavallini, G. Gallinaro, L. Meneghetti, G. Scoles, and M. Yealland, "Differential collision cross-section measurements in the elastic scattering of light identical molecules: Helium," *Phys. Rev. Lett.*, vol. 24, pp. 1469–1471, Jun 1970.

[43] J. M. Parson, P. E. Siska, and Y. T. Lee, "Intermolecular potentials from crossed-beam differential elastic scattering measurements. IV. Ar + Ar," *J. Chem. Phys.*, vol. 56, no. 4, pp. 1511–1516, 1972.

[44] M. L. Law and D. D. Fitts, "Comparison of Argon-Argon interatomic potentials from elastic molecular-beam scattering data," *Mol. Phys.*, vol. 29, no. 6, pp. 1933–1939, 1975.

[45] J. Hirschfelder, C. Curtiss, and R. Bird, *Molecular Theory of Gases and Liquids*. New York, NY: John Wiley and Sons, Inc., 1954.

[46] I. Gradshteyn, I. Ryzhik, and A. Jeffrey, *Table of Integrals, Series, and Products*. Academic Press, 6th ed., 2000.

[47] G. N. Watson, *A Treatise on the Theory of Bessel Functions.* Cambridge, England: University Press, 1962.

APPENDIX A

FTDS DERIVATION

1.1 The Radon Transform of the Velocity Vector Field

As discussed in Section 3.2, the inner product of the velocity vector $\mathbf{v}$ and probe direction $\hat{\mathbf{k}}_{\mathbf{probe}}$ results in the scalar projection w, equation A.1.

$$\mathbf{v} \cdot \hat{\mathbf{k}}_{\mathbf{probe}} = \|\mathbf{v}\| \cos \theta'' = w$$

$$\implies 0 = w - \mathbf{v} \cdot \hat{\mathbf{k}}_{\mathbf{probe}}$$

(A.1)

Each vector is defined by a particular set of coordinates, illustrated in Figure 29, about the principle axis of symmetry (the z-axis in our space-fixed coordinate system).
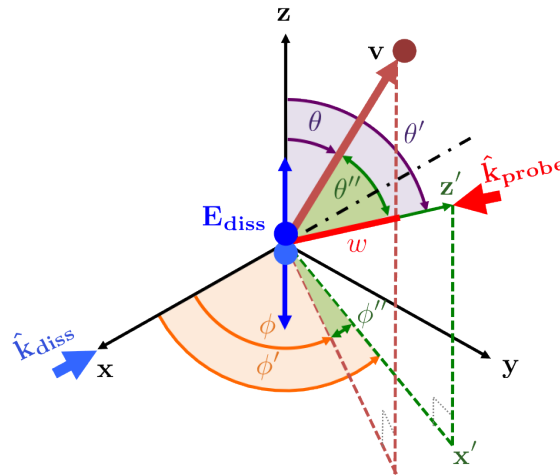
Figure 29. Space-fixed coordinate system for a parallel-type transition.

If a vector field $F(\mathbf{v})$ exists, such that a line impulse results from equation A.1, then the one-dimensional projection of the vector field, $D(w; \theta', \phi')$, is obtained by integrating $F(\mathbf{v})$ on a plane, whose orientation is described by $\hat{\mathbf{k}}_{\mathbf{probe}}$, the unit vector normal to the plane; Figure 30.
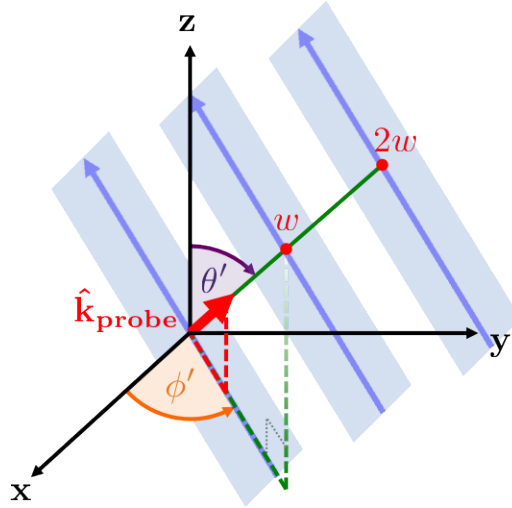
Figure 30. 3D projection geometry.

The projection $D(w; \theta', \phi')$ is also known as the Radon transform of $F(\mathbf{v})$, equation A.2.

$$D(w; \theta', \phi') = \int d^3\mathbf{v}\, F(\mathbf{v})\, \delta\big[w - \mathbf{v} \cdot \hat{\mathbf{k}}_{\mathbf{probe}}\big] \tag{A.2}$$

...where δ is the Dirac delta function defined by:

$$\delta[x] = 0 \iff x \neq 0$$
$$\implies \int_{-\infty}^{\infty} dx\, \delta[x] = 1 \tag{A.3}$$

This transformation maps the domain (v_x, v_y, v_z) to $(w; \hat{\mathbf{k}}_{\mathbf{probe}})$. The projection can be better seen and understood when mapping a two-dimensional object onto a line, Figures 31a and 31b.
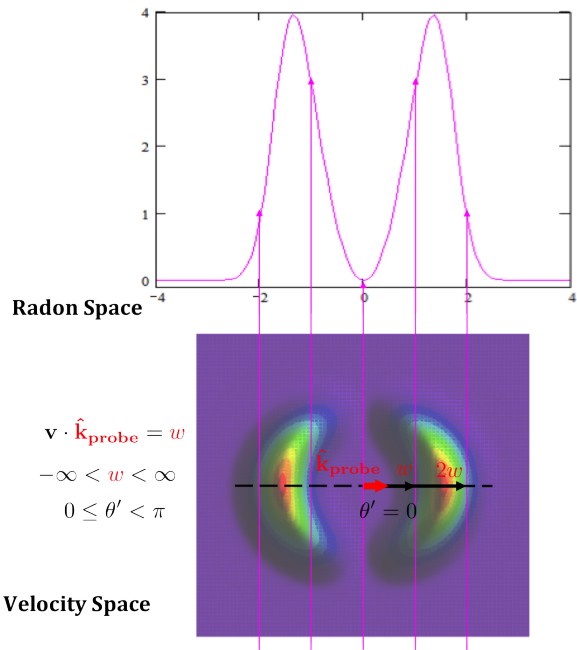
(a) Projection of $F(v, \theta)$ at $\theta' = 0$.
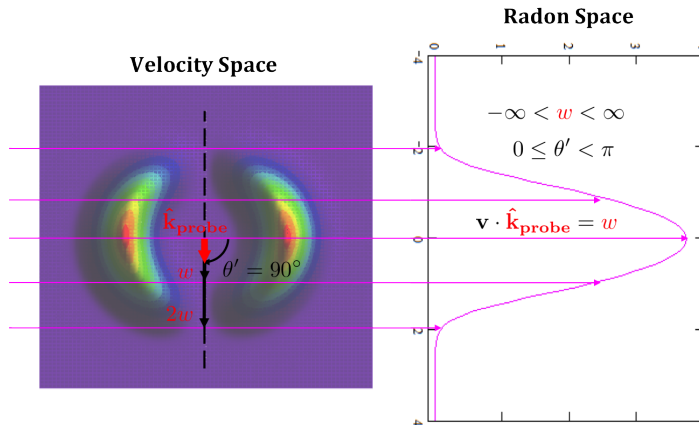
(b) Projection of $F(v, \theta)$ at $\theta' = \frac{\pi}{2}$.

Figure 31. Radon space projections of $F(v, \theta)$ at **a.)** $\theta' = 0$ and **b.)** $\theta' = \frac{\pi}{2}$.

1.2 Inverse Radon Transform: The Fourier Synthesis method

Figures 31a and 31b are simulated Doppler profiles of a parallel-type transition in photodissociation. The intent of FTDS is to invert Doppler profiles to acquire the velocity distribution of a two-body interaction. Since direct inversion of the Radon transform is difficult to derive and implement, an alternative method of inversion is through Fourier space [26]. Known as the Fourier synthesis method, this inversion is illustrated in Figure 32 and is based on the central-slice theorem.
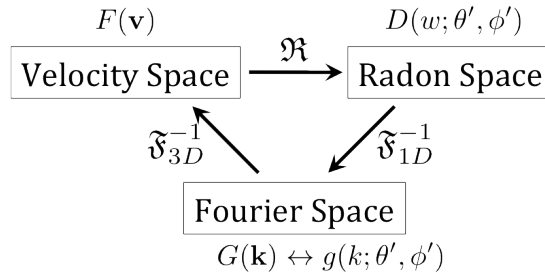
Figure 32. Central Slice Theorem.

The central-slice theorem states that the Fourier transform in w of a Radon projection, i.e. $D(w; \theta', \phi')$, at given angles is equal to the central line at the same angles of the Fourier transform of the original vector field, i.e. $F(\mathbf{v})$. For the FTDS derivation, we must assume $D(w; \theta', \phi')$ exists as a Fourier pair, equation A.4; where k is the conjugate variable of w.

$$g(k; \theta', \phi') = \int \mathrm{d}w \, D(w; \theta', \phi') \, e^{-2\pi i (kw)} \tag{A.4}$$

62

Insertion of equation A.2, the Radon transform of $F(\mathbf{v})$, into equation A.4, yields an expression that, in conjunction with the Fourier transform shift theorem, can be evaluated with respect to w.

$$g(k; \theta', \phi') = \int \mathrm{d}w \left[\int \mathrm{d}^3\mathbf{v} \, F(\mathbf{v}) \, \delta\big[w - \mathbf{v} \cdot \hat{\mathbf{k}}_{\mathbf{probe}} \big] \right] e^{-2\pi i(kw)} \tag{A.5}$$

Fourier Transform Shift Theorem

$$g(k; \theta', \phi') = \int \mathrm{d}^3\mathbf{v} \, F(\mathbf{v}) \left[\int \mathrm{d}w \, \delta\big[w - \mathbf{v} \cdot \hat{\mathbf{k}}_{\mathbf{probe}} \big] e^{-2\pi i(kw)} \right]$$

$$\tag{A.6}$$

$$g(k; \theta', \phi') = \int \mathrm{d}^3\mathbf{v} \, F(\mathbf{v}) \left[e^{-2\pi i(k)\mathbf{v} \cdot \hat{\mathbf{k}}_{\mathbf{probe}}} \right] \tag{A.7}$$

For a collection of unique central lines in Fourier space, the vector field can be reconstructed, where 3D Fourier transform of $F(\mathbf{v})$.

$$\implies g(k; \theta', \phi') = G(k \sin\theta' \cos\phi', k \sin\theta' \sin\phi', k \cos\theta')$$

$$G(\mathbf{k}) = \int \mathrm{d}^3\mathbf{v} \, F(\mathbf{v}) \, e^{-2\pi i \, \mathbf{k} \cdot \mathbf{v}} \tag{A.8}$$

The inverse 3D Fourier transform of equation A.8 recovers the space variant $F(\mathbf{v})$.

$$F(\mathbf{v}) = \int \mathrm{d}^3\mathbf{k} \, G(\mathbf{k}) \, e^{2\pi i \, \mathbf{k} \cdot \mathbf{v}} \tag{A.9}$$

1.3 Symmetric Distributions

The task of inverting a discrete set of angle-dependent Doppler profiles into its three-dimensional velocity distribution can be drastically simplified by considering the symmetry of the system.

Cylindrical Symmetry

In the case of collisions from crossed-molecular beams of well-defined velocities or photodissociation, cylindrical symmetry of the velocity distribution holds. The approximate axis of symmetry will pertain to the relative velocity direction in crossed-molecular beam studies and the electric vector of the dissociation laser in photodissociation, see Figure 12.

It is convenient to express the vectors $\mathbf{v}$ and $\mathbf{k}$ into their scalar components in spherical coordinates, see equation A.1:

$$F(v_x, v_y, v_z) = \int_{-\infty}^{\infty} dk_x \int_{-\infty}^{\infty} dk_y \int_{-\infty}^{\infty} dk_z \, G(k_x, k_y, k_z) \, e^{2\pi i \, (k_x v_x + k_y v_y + k_z v_z)}$$

$$F(v, \theta, \phi) = \int_0^{\infty} dk \, k^2 \int_0^{\pi} d\theta' \, \sin\theta' \int_0^{2\pi} d\phi' \, g(k; \theta', \phi')$$

$$\tag{A.10}$$

$$e^{2\pi i (k \sin\theta' \cos\phi')(v \sin\theta \cos\phi)} \, e^{2\pi i (k \sin\theta' \sin\phi')(v \sin\theta \sin\phi)} \, e^{2\pi i (k \cos\theta')(v \cos\theta)}$$

We can resolve the 3D Fourier transform in equation A.10 into a product of a 1D Fourier transform with respect to the axial direction, i.e. our "axis of symmetry," and a 2D Fourier transform in the "transverse plane." A radially symmetric 2D Fourier

transform is known as a Hankel transform of the zeroth order, also known as the Fourier-Bessel transform. This operation ostensibly allows us to ignore the ϕ' and ϕ in our problem.

$$D_{cyl}(w; \theta', \phi') = D_{cyl}(w; \theta')$$

$$g_{cyl}(k; \theta', \phi') = g_{cyl}(k; \theta')$$

Hankel transform of the zeroth order:

$$F(v, \theta) = \int_0^\infty \mathrm{d}k \, k^2 \int_0^\pi \mathrm{d}\theta' \, \sin\theta' \, g_{cyl}(k; \theta') \, e^{2\pi i(kv)\cos\theta'\cos\theta} \tag{A.11}$$

$$\cdot \left[\int_0^{2\pi} \mathrm{d}\phi' \, e^{2\pi i(kv)\sin\theta'\sin\theta\cos\phi'\cos\phi} \, e^{2\pi i(kv)\sin\theta'\sin\theta\sin\phi'\sin\phi} \right]$$

$$\int_0^{2\pi} \mathrm{d}\phi' \, e^{2\pi i(kv)\sin\theta'\sin\theta(\cos\phi'\cos\phi+\sin\phi'\sin\phi)}$$

Applying the trigonometric identity below results in the following operations:

$$\cos\phi'\cos\phi + \sin\phi'\sin\phi = \cos(\phi' - \phi)$$

$$\int_0^{2\pi} \mathrm{d}\phi' \, e^{2\pi i(kv)\sin\theta'\sin\theta\cos(\phi'-\phi)}$$

The variable ϕ can be removed by regarding it as a simple *phase shift*:

$$\int_{0-\phi}^{2\pi-\phi} \mathrm{d}\phi' \, e^{2\pi i(kv)\sin\theta'\sin\theta\cos\phi'}$$

The integral in equation A.11 is reduced to the zeroth order Bessel function of the first kind, $J_0(z)$, which sums the motion of the scattering products along the ϕ'-axis, reducing our 3D problem to 2D.

$$2\pi \left[\frac{1}{2\pi} \int_0^{2\pi} \mathrm{d}\phi' \, e^{2\pi i (kv) \sin \theta' \sin \theta \cos \phi'} \right] = 2\pi \left[J_0(2\pi kv \sin \theta' \sin \theta) \right] \qquad (A.12)$$

We can take the expression in equation A.12 and replace it with its counterpart in equation A.11 to obtain Kinsey's expression for a three-dimensional velocity distribution with cylindrical symmetry, equation A.13.

$$F(v, \theta) = 2\pi \int_0^\infty \mathrm{d}k \, k^2 \int_0^\pi \mathrm{d}\theta' \, \sin \theta' \, J_0(2\pi kv \sin \theta' \sin \theta) \, g_{cyl}(k; \theta') \, e^{2\pi i (kv) \cos \theta' \cos \theta}$$

$$(A.13)$$

Spherical Symmetry

In some cases, e.g. bulk gas phase samples, the collisions produce an isotropic distribution of scattering products. This translates into an apparent likelihood that all components of the velocity vector have the same frequency of occurrence and are weighted the same in each direction; i.e. $v_x = v_y = v_z$. Therefore, the spherically symmetric scattering system is a one-dimensional problem, equation A.14. Considering

the illustration in Figure 12 and if $v_z = v\cos\theta'' = w$, where $\cos\theta'' = 1$, then:

$$D(w) = \int \mathrm{d}^3\mathbf{v}\, F(\mathbf{v})\, \delta\big[w - \mathbf{v}\cdot\hat{\mathbf{k}}_{\mathbf{probe}}\big]$$

$$= \frac{1}{4\pi}\int_{-\infty}^{\infty}\mathrm{d}v_x \int_{-\infty}^{\infty}\mathrm{d}v_y \int_{-\infty}^{\infty}\mathrm{d}v_z\, f\big(\sqrt{v_x^2 + v_y^2 + v_z^2}\big)\,\delta\big[w - v_z\big] \qquad (\text{A.14})$$

$$v_z = w$$

$$= \frac{1}{4\pi}\int_{-\infty}^{\infty}\mathrm{d}v_x \int_{-\infty}^{\infty}\mathrm{d}v_y\, f\big(\sqrt{v_x^2 + v_y^2 + w^2}\big) \int_{-\infty}^{\infty}\mathrm{d}v_z \delta\big[w - v_z\big]$$

Consider the polar coordinates in the v_x–v_y plane

$$v_x = u\cos\phi$$

$$v_y = u\sin\phi$$

$$v^2 = u^2 + w^2$$

$$= \frac{1}{4\pi}\int_{u=0}^{\infty}\mathrm{d}u\, u \int_{\phi=0}^{2\pi}\mathrm{d}\phi\, f\big(\sqrt{u^2 + w^2}\big) = \frac{2\pi}{4\pi}\int_{u=0}^{\infty}\mathrm{d}u\, u\, f\big(\sqrt{u^2 + w^2}\big) \quad (\text{A.15})$$

$$\text{If... } u = \sqrt{v^2 - w^2} \implies \mathrm{d}u = \frac{\frac{1}{2}}{\sqrt{v^2-w^2}}\,(2v)\,\mathrm{d}v$$

$$u\mathrm{d}u = v\mathrm{d}v$$

$$\text{...then, as } u \to 0 \implies v = (w^2)^{\frac{1}{2}} \text{ and...}$$

$$D(w) = \frac{1}{2}\int_{v=|w|}^{\infty}\mathrm{d}v\, v\, f(v) \quad \text{...where } w > 0 \qquad (\text{A.16})$$

Equation A.16 suggests:

$$\left[\frac{\mathrm{d}D(w)}{\mathrm{d}w} \right]_{w=v} = -\frac{1}{2v} \, v^2 f(v) \qquad (A.17)$$

APPENDIX B

DERIVATION OF GENERAL METHOD

2.1 An Analytical Form for the Doppler Profile

Taatjes *et al.* in 1990 developed a method to recover cylindrically symmetric velocity distributions by solving Kinsey's Fourier transform analytically. This method utilizes an expansion for the Doppler profile in classical orthogonal polynomials, equation B.1. The use of classical orthogonal polynomials is intentional due to their known transform properties, equation B.2.

$$D_{cyl}(w; \theta') = \sum_l P_l(\cos \theta') \sum_n a_{l,n} H_n(w) e^{-w^2} \tag{B.1}$$

$$g_{cyl}(k; \theta') = \int_{-\infty}^{\infty} dw \, D_{cyl}(w; \theta') e^{-2\pi i(kw)}$$

$$= \sum_l P_l(\cos \theta') \sum_n a_{l,n} \int_{-\infty}^{\infty} dw \, H_n(w) e^{-w^2} e^{-2\pi i(kw)} \tag{B.2}$$

Equation B.3 is the evaluated integral in equation B.2, obtained from Gradshteyn *et al.* [46].

$$\int_{-\infty}^{\infty} dx \, H_n(x) e^{-(x-y)^2} = \sqrt{\pi}(y)^n 2^n$$

$$\int_{-\infty}^{\infty} dw \, H_n(w) e^{-w^2} e^{-2\pi i(kw)} = \sqrt{\pi}(-i)^n (2\pi k)^n e^{-\pi^2 k^2}$$

$$\Longrightarrow \ x = w \text{ and } y = -i\pi k$$

$$g_{cyl}(k; \theta') = \sum_l P_l(\cos \theta') \sum_n a_{l,n} \left[\sqrt{\pi}(-i)^n (2\pi k)^n e^{-\pi^2 k^2} \right] \tag{B.3}$$

In photodissociation, the Doppler profiles are symmetric about ν_0, and therefore, require only an expansion in even Hermite terms, however, odd terms can easily be incorporated for asymmetric profiles; generalized in equation B.3. Equation B.4 is obtained by replacing the $g_{cyl}(k; \theta')$ in Kinsey's 3D Fourier transform, equation A.13, with the expression derived in equation B.3.

$$F(v, \theta) = 2\pi \int_0^\infty dk\, k^2 \int_0^\pi d\theta'\, \sin \theta'\, J_0(2\pi k v \sin \theta' \sin \theta)\, e^{2\pi i (kv) \cos \theta' \cos \theta}$$
$$\cdot \sum_l P_l(\cos \theta') \sum_n a_{l,n} \left[\sqrt{\pi}(-i)^n (2\pi k)^n e^{-\pi^2 k^2} \right] \tag{B.4}$$

Due to the linearity of the integral operator, a one-to-one correspondence exists between the Doppler profile and its velocity distribution. Therefore, an expansion in Legendre terms for the Doppler profile corresponds to the same Legendre terms in our velocity distribution. As a result of this property, we can evaluate each Legendre term on a term by term basis, equation B.5.

$$F(v, \theta) = \sum_l F_l(v, \theta)$$

$$F_l(v,\theta) = 2\pi \int_0^\infty \mathrm{d}k\, k^2 \int_0^\pi \mathrm{d}\theta' \, \sin\theta' \, J_0(2\pi k v \sin\theta' \sin\theta)\, e^{2\pi i(kv)\cos\theta' \cos\theta}$$

$$\cdot P_l(\cos\theta') \sum_n a_{l,n} \left[\sqrt{\pi}(-i)^n (2\pi k)^n \, e^{-\pi^2 k^2} \right] \tag{B.5}$$

Evaluating with respect to θ' results in equation B.6; obtained from the Gegenbauer's finite integral [47].

$$\int_0^\pi e^{i(z)\cos\theta\cos\phi} J_{v-\frac{1}{2}}(z\sin\theta\sin\phi) \cdot C_r^v(\cos\theta) \sin^{v+\frac{1}{2}}\theta \, \mathrm{d}\theta$$

$$= \left(\frac{2\pi}{z}\right)^{\frac{1}{2}} i^r \sin^{v-\frac{1}{2}}\phi \cdot C_r^v(\cos\phi) J_{v+r}(z) \tag{B.6}$$

$$v - \frac{1}{2} = 0 \implies v = \frac{1}{2}, \; r = l, \; z = 2\pi i k v$$

We use a special case of Gegenbauer's finite integral, where the Gegenbauer polynomial $C_r^v(\cos\theta)$ reduces to the Legendre polynomial, $P_l(\cos\theta)$; equation B.7

$$\int_0^\pi e^{2\pi i(kv)\cos\theta'\cos\theta} J_0(2\pi i \sin\theta' \sin\theta) \cdot P_l(\cos\theta') \sin\theta' \, \mathrm{d}\theta'$$

$$= \left(\frac{1}{kv}\right)^{\frac{1}{2}} i^l \cdot P_l(\cos\theta) J_{\frac{1}{2}+l}(2\pi kv) \tag{B.7}$$

The resultant expression in equation B.7 can be placed into equation B.5 and simplified; see equation B.8.

$$F_l(v,\theta) = 2\pi \int_0^\infty \mathrm{d}k\, k^2 \left[\left(\frac{1}{kv}\right)^{\frac{1}{2}} i^l \cdot P_l(\cos\theta) J_{\frac{1}{2}+l}(2\pi kv) \right] \sum_n a_{l,n} \sqrt{\pi}(-i)^n (2\pi k)^n \, e^{-\pi^2 k^2}$$

$$F_l(v, \theta) = 2(\pi)^{\frac{3}{2}} \, v^{-\frac{1}{2}} \, i^l \cdot P_l(\cos\theta) \sum_n a_{l,n} \, (-i)^n (2\pi)^n \int_0^\infty \mathrm{d}k \, k^{n+\frac{3}{2}} \, e^{-\pi^2 k^2} J_{\frac{1}{2}+l}(2\pi k v)$$

$$(B.8)$$

Obtained from *Bessel functions, exponentials and powers* in Gradshteyn *et al.* [46], evaluating $\mathrm{d}k$ in equation B.8 produces equation B.9:

$$\int_0^\infty \mathrm{d}x \, x^\mu \, e^{-\alpha x^2} \, J_v(\beta x) = \frac{\Gamma\left(\frac{v}{2} + \frac{\mu}{2} + \frac{1}{2}\right)}{\beta \, \alpha^{\frac{\mu}{2}} \, \Gamma(v+1)} \, e^{\left(-\frac{\beta^2}{8\alpha}\right)} \cdot M_{\frac{\mu}{2},\frac{v}{2}}\left(\frac{\beta^2}{4\alpha}\right)$$

Whittaker's Function

$$M_{\frac{\mu}{2},\frac{v}{2}}\left(\frac{\beta^2}{4\alpha}\right) = e^{-\left(\frac{\beta^2}{8\alpha}\right)} \left(\frac{\beta^2}{4\alpha}\right)^{\frac{1}{2}(v+1)} {}_1F_1\left(\frac{1+v-\mu}{2}; 1+v; \frac{\beta^2}{4\alpha}\right)$$

$$\implies \mu = n + \frac{3}{2}, \ \alpha = \pi^2, \ v = \frac{1}{2} + l, \ \beta = 2\pi v, \ x = k$$

$$\int_0^\infty \mathrm{d}k \, k^{n+\frac{3}{2}} \, e^{-\pi^2 k^2} \, J_{\frac{1}{2}+l}(2\pi v k)$$

$$= \frac{\Gamma\left(\frac{3+n+l}{2}\right)}{(2\pi v) \, \pi^{\left(n+\frac{3}{2}\right)} \, \Gamma(\frac{3}{2}+l)} \, e^{-v^2} \, v^{\frac{3}{2}+l} \, {}_1F_1\left(\frac{l-n}{2}; \frac{3}{2}+l; v^2\right) \qquad (B.9)$$

The resultant expression in equation B.9can be placed back into equation B.8 and simplified; equation B.10. Equation B.10 is our analytical expression for recovering a cylindrically symmetric three-dimensional velocity distribution via FTDS.

$$F_l(v, \theta) = 2\pi^{\frac{3}{2}} \, v^{-\frac{1}{2}} \, i^l \cdot P_l(\cos\theta) \sum_n a_{l,n} \, (-i)^n (2\pi)^n$$

$$\frac{\Gamma\left(\frac{3+n+l}{2}\right)}{(2\pi v) \, \pi^{\left(n+\frac{3}{2}\right)} \, \Gamma(\frac{3}{2}+l)} \, e^{-v^2} \, v^{\frac{3}{2}+l} \, {}_1F_1\left(\frac{l-n}{2}; \frac{3}{2}+l; v^2\right)$$

$$F_l(v, \theta) = \frac{i^l \, v^l \, e^{-v^2} \, P_l(\cos\theta)}{\pi \, \Gamma\!\left(\frac{3}{2} + l\right)} \sum_n a_{l,n} \, (-i)^n \, 2^n \, \Gamma\!\left(\frac{3 + n + l}{2}\right) \, {}_1F_1\!\left(\frac{l - n}{2}; l + \frac{3}{2}; v^2\right)$$

<div align="right">(B.10)</div>

2.2 Solving for the Expansion Coefficients

Taatjes' method for solving the integral transform analytically utilizes the coefficients of the Doppler profile expansion in terms of Hermite and Legendre polynomials, which directly gives the coefficients of the velocity distribution in terms of other known functions. Below are the normalized classical orthogonal polynomials used in this expansion:

Orthogonality of Legendre Polynomials

$$\int_{-1}^{1} \mathrm{d}x \, P_k(x) \, P_l(x) = \frac{2}{2l + 1} \, \delta_{k,l}$$

$$\int_{\pi}^{0} \mathrm{d}(\cos\theta') \, P_k(\cos\theta') \, P_l(\cos\theta') = \frac{2}{2l + 1} \, \delta_{k,l}$$

$$\int_{0}^{\pi} \mathrm{d}\theta' \, \sin\theta' \, P_k(\cos\theta') \, P_l(\cos\theta') = \frac{2}{2l + 1} \, \delta_{k,l}$$

Orthogonality of Hermite Polynomials

$$\int_{-\infty}^{\infty} \mathrm{d}w \, H_m(w) \, H_n(w) \, e^{-w^2} = \sqrt{\pi} \, 2^n \, n! \, \delta_{m,n}$$

Equation B.11 is the product of normalized Legendre and Hermite polynomials:

$$\frac{1}{\sqrt{\pi} \, 2^n \, n!} \frac{2l + 2}{2} \int_{-\infty}^{\infty} \mathrm{d}w \int_{0}^{\pi} \mathrm{d}\theta' \, \sin\theta' \, H_m(w) \, H_n(w) \, e^{-w^2} \, P_k(\cos\theta') \, P_l(\cos\theta') = \delta_{k,l} \, \delta_{m,n}$$

<div align="right">(B.11)</div>

In solving for the coefficients, we must assume $D_{cyl}(w; \theta')$ is gaussian in nature over the interval of interest, only then can the coefficients for the expansion be obtained using equation B.1; see equation B.12.

$$\frac{1}{\sqrt{\pi}\, 2^n\, n!} \frac{2l+2}{2} \int_{-\infty}^{\infty} dw \int_0^{\pi} d\theta'\, \sin\theta'\, D_{cyl}(w; \theta')\, H_n(w)\, P_l(\cos\theta') = a_{l,n}\, \delta_{k,l}\, \delta_{m,n}$$

$$(B.12)$$

$$\frac{1}{\sqrt{\pi}\, 2^n\, n!} \frac{2l+2}{2} \int_{-\infty}^{\infty} dw \int_0^{\pi} d\theta'\, \sin\theta' \left[\sum_l P_l(\cos\theta') \sum_n a_{l,n}\, H_n(w)\, e^{-w^2} \right]$$
$$H_n(w)\, P_l(\cos\theta') = a_{l,n}$$

$$\frac{a_{l,n}}{\sqrt{\pi}\, 2^n\, n!} \frac{2l+2}{2} \int_{-\infty}^{\infty} dw \int_0^{\pi} d\theta'\, \sin\theta'\, P_l(\cos\theta')\, H_n(w)\, e^{-w^2}\, H_n(w)\, P_l(\cos\theta') = a_{l,n}$$